Construction and characterization of a multi-antenna terahertz time-domain spectroscopy setup

by

Shane Raymond Smith

Thesis presented in partial fulfilment of the requirements for the degree of Masters of Science in Laser Physics in the Faculty of Nature Science at Stellenbosch University

Department of Physics,
Stellenbosch University ,
Private Bag X1, Matieland 7602, South Africa.

Supervisor: Dr. P.H. Neethling Co-supervisor: Prof. E.G. Rohwer

March 2015

Declaration

By submitting this thesis electronically, I declare that the entirety of the work contained therein is my own, original work, that I am the sole author thereof (save to the extent explicitly otherwise stated), that reproduction and publication thereof by Stellenbosch University will not infringe any third party rights and that I have not previously in its entirety or in part submitted it for obtaining any qualification.

Date: .....

Uittreksel

Ontwikkeling en karakterisering van 'n tyd verwante multi-antenna terahertz spektroskopie sisteem

("Construction and characterization of a multi-antenna terahertz time-domain spectroscopy setup")

S.R. Smith

Departement Fisika,
Universiteit Stellenbosch,
Privaatsak X1, Matieland 7602, Suid Afrika.

Tesis: MSc (Physics)

Maart 2015

Danksê onlangse tegnologiese onwikkelings in lasers en halfgeleier het dit veel makliker geraak om terahertz straling te genereer wat fase samehangendheid toon. Voor hierdie ontwikkelings was straling in hierdie spektrale gebied moeilik om te genereer op 'n wyse wat fase samehangendheid toon.

Tyd verwante terahertz spektroskopie is taamlik uniek, aangesien die metings in tyd geneem word en die elektriese veld amplitude word pleks van die intensiteit gemeet.

Een van die voordele van hierdie metode is dat dit toelaat vir die meeting van die komplekse brekingsindeks van monsters. Dit is moontlik om van die komplekse brekingsindeks strukturele en omgewings eienskappe van die monster af te lei.

Gedurende die projek was 'n tyd verwante terahertz spektroskopie sisteem gebou wat gebaseer was op lae temperatuur gegroeide GaAs foto-geleidende antennas. Die sisteem bevat vier antennas van verskillende groottes aan beide die sender en ontvanger kant.

Die antennas was gekarakteriseer na die bou en belyning van die terahertz sisteem en meetings was gedoen op die agtergrond, suiker en silikon om die sisteem se vermoë te demonstreer.

Dit was gevind dat die amplitude van die gemete terahertz elektriese veld groter geraak het soos die intensiteit van die pomp puls verhoog was en dat die die amplitude van die gemete terahertz electriese veld afhanklik was van die polarisasie van die pomp puls. Die amplitude van van die gemete terahertz

elektriese veld het gegroei met die grootte van die antenna, maar hoe groter die antenna geraak het, hoe kleiner was die bandwydte van die gemete terahertz elektriese veld. Hierdie was die geval vir beide die sender en ontvanger antennas.

Abstract

Construction and characterization of a multi-antenna terahertz time-domain spectroscopy setup

S.R. Smith

Department of Physics,
Stellenbosch University ,
Private Bag X1, Matieland 7602, South Africa.

Thesis: MSc (Fisika)

March 2015

Recent progress in laser and semiconductor technology has allowed for far easier generation and measuring of coherent terahertz radiation, a previously difficult region in the radiation spectrum to coherently generate.

Time based terahertz spectroscopy is a rather unique form of spectroscopy. Not only is it time based, but the electric field is measured instead of the intensity.

This allows for the measurement of the complex refractive index. From this one can obtain certain details of the structure and environment of the sample being studied.

A terahertz time-domain spectroscopy setup was constructed during this project. This setup used low temperature grown GaAs photoconductive antennae, with multiple antenna size options available for both the receiving and transmitting antennae.

After the construction and alignment of this setup, the antennae were characterized.

Lastly measurements were performed on the background, sugar and silicon to demonstrate the capabilities of the system.

It was found that the measured terahertz electric field amplitude increased with the intensity of the pump pulse and that the amplitude of the measured terahertz electric field was dependent on the polarization of the pump pulse. As the size of the antenna was increased so too did the amplitude of the measured electric field and conversely the bandwidth of the measured terahertz electric field decreased with the increase of antenna size. This held true for both the transmitting and receiving antennae.

Acknowledgements

I would like to express my sincere gratitude to the following people and organizations. To my supervisor, Dr P.H. Neethling, and co-supervisor, Prof E.G. Rohwer, for their continued help.

To L. Conradie, for lending us a lock-in amplifier that was used during the early stages of this thesis.

The financial assistance of the National Research Foundation (NRF) towards this research is hereby acknowledged. Opinions expressed and conclusions arrived at, are those of the author and are not necessarily to be attributed to the NRF.

Contents

List of Figures

List of Tables

Nomenclature

Constants

c =	$2.998 \times 10^8\,\mathrm{m/s}$
μ_0 =	$4\pi \times 10^{-7}\,\mathrm{Wb/A\ m}$
ϵ_0 =	$8.85419 \times 10^{-12}\,\mathrm{C^2/J\ m}$

Variables

r	Coordinate	[m]
θ	Rotation angle	[rad]
q	Charge	[C]
ω	angular frequency	[rad/s]
t	time	[s]
α	absorption coefficient	[$\mathrm{cm^{-1}}$]
E	Electric field	[V/m]
B	Magnetic field	[T]
D	Electric Auxiliary field	[$\mathrm{C/m^2}$]
H	Magnetic Auxiliary field	[A/m]
V	Scalar Potential	[V]
$\vec{A}$	Vector Potential	[V]

Chapter 1

Introduction

Terahertz radiation lies between far infrared and microwave radiation in the electromagnetic spectrum, and is generally seen as being from $0.3 - 10\,\text{THz}$. This area can also be seen as the border between optical and electronic wavelengths.

Terahertz radiation has been of interest to the physics community since the end of the 1920s. One of the sources of this interest is due to terahertz radiation applications in astronomy. According to results from NASA's Diffuse Infrared Background Experiment and examination of the spectral energy distributions in observable galaxies, approximately half of the luminosity and 98% of the photons emitted since the Big Bang fall into the terahertz and far-IR spectrum. Most of this radiation is being emitted by cool interstellar dust, of which older galaxies, such as the Milky Way, have a much greater abundance. Thus, terahertz detectors make for true probes into the early universe [3] - [5].

Another reason for interest in terahertz radiation is the strength of the absorption lines displayed by lightweight molecules, such as CO and water, in this spectrum, thus making terahertz well suited to spectroscopy of lightweight molecules [3].

One of the key difficulties when trying to detect terahertz radiation, as compared to visible light, is the low photon energy of this spectrum (about $1-42\,\text{meV}$), which means that ambient background thermal noise will generally dominate naturally emitted narrow-band signals.

When comparing with longer wavelength radio techniques, terahertz detectors suffer from not having similar electronic components available, such as amplifiers [3].

Until recently, heterodyne detectors have been the most common terahertz detectors [3]. These are semiconducting detectors that make use of difference frequency mixing to perform terahertz detection. Generally optically pumped gas lasers were used to produce the reference radiation for the mixer [6]. These detectors can be rather expensive and due to the need for a reference radiation generator it can be quite large.

In the past, before ultrafast lasers became readily available, terahertz generation has been problematic. Traditional electronic sources show too much losses at higher frequencies which make them poor terahertz generators and optical sources must operate at energy levels so low that they are comparable with that of the lattice phonons of the semiconductor. Using cryogenic cooling it is possible to work around this problem. Making use of nonlinear crystals, lasing gasses and quantum cascade lasers have had more success [3]. Synchrotrons have also been used as terahertz radiation sources.

With the advent of readily available ultrafast lasers and advances in semiconductor technology there has been quite a boom in terahertz technology in recent years. Two new types of detectors rapidly gained a lot of ground in the field, namely photoconductive antennae and electro-optical crystals. Photoconductive antennae can also function as terahertz generators and certain electro-optical crystals, such as ZnTe, can facilitate optical rectification, which also allows for terahertz generation [7]. These advances in terahertz technology allowed for the construction of more compact terahertz setups and at a rather lower cost than previously possible.

Two other terahertz generation methods have also received a lot of attention in recent years, namely optical rectification via a plasma and quantum cascade lasers. Quantum cascade lasers show great promise in fields where a higher intensity terahertz pulse is preferable to a large bandwidth, since they are capable of producing high intensity, small bandwidth pulses [7; 8].

Electro-optical crystals and photoconductive antennae show similar performance in terms of bandwidth, resolution and intensity [7]. Although electro-optical crystals are less sensitive to alignment than photoconductive antennae, the bandwidth of the radiation they generate via optical rectification is far more dependent on the pulse duration of the ultrafast laser used to pump them. The case of plasma based terahertz sources is similar to that of electro-optical crystals.

For certain purposes, such as examining biological samples or semiconductor samples more exotic methods such as ellipsometry and pump-probe experiments might be preferable to conventional transmission spectroscopy. To do

this a foundation in how to align a terahertz setup and a relatively versatile terahertz time-domain setup is preferable.

During this thesis a terahertz time-domain spectroscopy setup will be constructed. This will be done to help develop the skills needed to align a terahertz setup and to have a setup that will be ready for further expansion or alteration. This setup will incorporate photoconductive antennae and will make use of multiple antennae. These antennae will be characterized as part of this project, so as to gain further understanding on how to optimally construct a terahertz time-domain spectroscopy setup and be able to perform reliable and predictable measurements.

1.1 Objectives

- Design and construct a terahertz time-domain spectroscopy setup.
- Characterize the photoconductive antennae available for use.
- Take measurements to demonstrate the capabilities of the system.

1.2 Thesis structure

Chapter 2: Background theory on light-matter interaction is discussed in this chapter.
Chapter 3: Two methods of terahertz generation and detection are discussed in this chapter, namely photoconductive antennae and electro-optical crystals.
Chapter 4: This chapter contains details on the design and construction of the terahertz time-domain spectroscopy setup. In this chapter, the techniques used to construct and align this setup are also highlighted.
Chapter 5: The results obtained from characterizing the photoconductive antennae are discussed in this chapter. Some examples of spectroscopic measurements performed on samples are also shown, as well as complex refractive index data extracted from these measurements. The examples used are atmospheric water vapor, a thin sugar crystal and a silicon wafer.

Chapter 2

Background theory

Before delving into the intricacies of terahertz time-domain spectroscopy, it is important to understand how electro-magnetic radiation interacts with matter. In this chapter a base theory for light-matter interaction will be discussed.

2.1 Electro-magnetic radiation

Electro-magnetic radiation when viewed in a classical manner can be seen as a wave. For most descriptions in this thesis this will be a sufficient description.

According to Griffiths *et al.* [1], the propagation of electromagnetic waves can be described using Maxwell's equations:

$$\vec{\nabla} \cdot \vec{E} = \frac{1}{\epsilon_0}\rho \tag{2.1.1}$$

$$\vec{\nabla} \cdot \vec{B} = 0 \tag{2.1.2}$$

$$\vec{\nabla} \times \vec{E} = -\frac{\partial \vec{B}}{\partial t} \tag{2.1.3}$$

$$\vec{\nabla} \times \vec{B} = \mu_0 \vec{J} + \mu_0 \epsilon_0 \frac{\partial \vec{E}}{\partial t}. \tag{2.1.4}$$

Where ρ is the charge density of the medium through which the electro-magnetic wave propagates and $\vec{J}$ is the current density of the medium.

In the case of a vacuum, since ρ and $\vec{J}$ disappear, equations 2.1.1-2.1.4 become [1]:

$$\vec{\nabla} \cdot \vec{E} = 0 \tag{2.1.5}$$
$$\vec{\nabla} \cdot \vec{B} = 0 \tag{2.1.6}$$
$$\vec{\nabla} \times \vec{E} = -\frac{\partial \vec{B}}{\partial t} \tag{2.1.7}$$
$$\vec{\nabla} \times \vec{B} = \mu_0 \epsilon_0 \frac{\partial \vec{E}}{\partial t}. \tag{2.1.8}$$

This forms the basis on which the rest of the theory discussed in this chapter will be built.

2.2 Electric dipole radiation

Consider two spheres with opposite charges (at time t their charges are $q(t)$ and $-q(t)$) a distance d from one another. If the charge between these two spheres is then driven, for instance by an electric field, at an angular frequency ω ($q(t) = q_0 \cos \omega t$), this will result in the system becoming an oscillating electric dipole:

$$\vec{p}(t) = p_0 \cos(\omega t)\hat{z}$$

where:

$$p_0 = q_0 d$$

is the maximum value of the dipole moment.

If this is approximated to be a perfect dipole (the separation distance d between the two charges is considered to be very small ($d << r$)), in the perfect dipole limit ($d << \frac{c}{\omega}$) and at a relatively large distance from the source. Since the travel time of the electric field to the two charge carriers needs to be factored in when calculating the induced potential, the retarded potential is used. This retarded potential is given by:

$$V(r, \theta, t) = -\frac{p_0 \omega}{4\pi\epsilon_0 c}\left(\frac{\cos(\theta)}{r}\right)\sin[\omega(t - r/c)]$$

.
Using the current flowing between the spheres ($\vec{I}(t) = \frac{dq}{dt}\hat{z}$) and by approximating that this is a perfect dipole and in the perfect dipole limit, the vector potential is given by:

$$\vec{A}(r, \theta, t) = -\frac{\mu_0 p_0 \omega}{4\pi c}\left(\frac{\cos(\theta)}{r}\right)\sin[\omega(t - r/c)]\hat{z}.$$

From these two potentials the fields can be calculated:

$$\vec{E} = -\vec{\nabla}V - \frac{\partial \vec{A}}{\partial t}$$

$$\vec{B} = \vec{\nabla} \times \vec{A}$$

where:

$$\begin{aligned} \vec{\nabla}V &= \frac{\partial V}{\partial r}\hat{r} + \frac{1}{r}\frac{\partial V}{\partial \theta}\hat{\theta} \\ &\cong \frac{p_0\omega^2}{4\pi\epsilon_0 c^2}\left(\frac{\cos(\theta)}{r}\right)\cos[\omega(t-r/c)]\hat{r} \end{aligned}$$

$$\frac{\partial \vec{A}}{\partial t} = \frac{\mu_0 p_0 \omega^2}{4\pi r}\cos[\omega(t-r/c)](\cos\theta\hat{r} - \sin\theta\hat{\theta}).$$

Thus:

$$\vec{E} = -\frac{\mu_0 p_0 \omega^2}{4\pi}\left(\frac{\sin\theta}{r}\right)\cos[\omega(t-r/c)]\hat{\theta} \tag{2.2.1}$$

$$\vec{B} = -\frac{\mu_0 p_0 \omega^2}{4\pi c}\left(\frac{\sin\theta}{r}\right)\cos[\omega(t-r/c)]\hat{\phi}. \tag{2.2.2}$$

The energy radiated by an electric dipole is given by the Poynting vector:

$$\vec{S} = \frac{1}{\mu_0}(\vec{E}\times\vec{B}) = \frac{\mu_0}{c}\left\{\frac{p_0\omega^2}{4\pi}\left(\frac{\sin\theta}{r}\right)\cos[\omega(t-r/c)]\right\}^2\hat{r}. \tag{2.2.3}$$

Averaging the Poynting vector in time gives the intensity:

$$\left\langle \vec{S} \right\rangle = \left(\frac{\mu_0 p_0^2 \omega^4}{32\pi^2 c}\right)\frac{\sin^2\theta}{r^2}\hat{r}. \tag{2.2.4}$$

It can be seen from this equation that there is no radiation along the axis of the dipole ($\sin\theta = 0$). The total radiated power can be found by integrating $\left\langle \vec{S} \right\rangle$ over a sphere of radius r [1]:

$$\langle P \rangle = \frac{\mu_0 p_0^2 \omega^4}{12\pi c}. \tag{2.2.5}$$

2.3 Dielectrics

When an electric field is applied to a dielectric it produces dipoles in the material. The reason for this is that the electric field distorts the charge distribution in each atom of the material. The pull of the electric field on the electrons and the nucleus are in the opposite directions, since they possess

opposing charges. These negative and positive charges are still attracted to each other, and thus there is a pulling force between them. Once equilibrium is reached between these two forces, the atom is polarized, thus, leaving a small separation between the centroids of the positive and negative charge distributions. This, then leaves the atom with an induced dipole moment [9].

2.4 Light-matter interaction

It can be shown that within matter with no free charge or current Maxwell's equations (equations 2.1.1-2.1.4) become:

$$\vec{\nabla} \cdot \vec{D} = 0 \tag{2.4.1}$$
$$\vec{\nabla} \cdot \vec{B} = 0 \tag{2.4.2}$$
$$\vec{\nabla} \times \vec{E} = -\frac{\partial \vec{B}}{\partial t} \tag{2.4.3}$$
$$\vec{\nabla} \times \vec{H} = \frac{\partial \vec{D}}{\partial t}. \tag{2.4.4}$$

For linear, homogeneous matter $\vec{D} = \epsilon \vec{E}$ and $\vec{H} = \frac{1}{\mu}\vec{B}$, thus the Maxwell equations reduce to:

$$\vec{\nabla} \cdot \vec{E} = 0 \tag{2.4.5}$$
$$\vec{\nabla} \cdot \vec{B} = 0 \tag{2.4.6}$$
$$\vec{\nabla} \times \vec{E} = -\frac{\partial \vec{B}}{\partial t} \tag{2.4.7}$$
$$\vec{\nabla} \times \vec{B} = \mu\epsilon\frac{\partial \vec{E}}{\partial t}. \tag{2.4.8}$$

If this is compared to Maxwell's equations for electromagnetic waves propagating in vacuum (equations 2.1.5 to 2.1.8), it can be seen that the only difference is that $\mu_0\epsilon_0$ has been replaced by $\mu\epsilon$. From this it can be deduced that the wave is no longer moving at $c = \frac{1}{\sqrt{\mu_0\epsilon_0}}$, but instead at a reduced velocity, $v = \frac{1}{\sqrt{\mu\epsilon}}$.

This ratio in velocities is denoted as the index of refraction ($n = \sqrt{\frac{\epsilon\mu}{\epsilon_0\mu_0}}$).

In order to build a full image of how electro-magnetic radiation and matter interact, it is important to understand what happens at the boundary between two different materials. According to Griffiths *et al.* [1] it can be shown that the following boundary conditions for electro-magnetic radiation exist where

two different materials meet:

$$\epsilon_1 E_1^{\perp} = \epsilon_2 E_2^{\perp} \tag{2.4.9}$$

$$E_1^{\parallel} = E_2^{\parallel} \tag{2.4.10}$$

$$\frac{1}{\mu_1} B_1^{\parallel} = \frac{1}{\mu_2} B_2^{\parallel} \tag{2.4.11}$$

$$B_1^{\perp} = B_2^{\perp} \tag{2.4.12}$$

where $E^{\perp}$ and $B^{\perp}$ are the electric and magnetic field components polarized perpendicular to the plain of incidence and $E^{\parallel}$ and $B_1^{\parallel}$ are the electric and magnetic field components polarized parallel to the plain of incidence. These equations give the details for transmitted and reflective electromagnetic waves which form when light moves from one transparent[1] media to another. These conditions are deduced from Maxwell's equations.

Via further calculations, according to Griffiths *et al.* [1], it is possible to derive from these equations the Fresnel equations:

$$\widetilde{E}_{0R} = \left(\frac{a-\beta}{a+\beta}\right) \widetilde{E}_{0I} \tag{2.4.13}$$

$$\widetilde{E}_{0T} = \left(\frac{2}{a+\beta}\right) \widetilde{E}_{0I} \tag{2.4.14}$$

with:

$$a = \frac{\cos\theta_T}{\cos\theta_I} \tag{2.4.15}$$

and

$$\beta = \frac{\mu_1 v_1}{\mu_2 v_2} = \frac{\mu_1 n_2}{\mu_2 n_1} \tag{2.4.16}$$

where $\widetilde{E}_{0I}$ is the electric field incident on the boundary between the two materials, $\widetilde{E}_{0R}$ and $\widetilde{E}_{0T}$ are the electric fields reflected off and transmitted through this boundary and μ_1 and μ_2 are the magnetic permeability of the respective materials. In the case of dielectric materials both μ_1 and μ_2 can be approximated as μ_0, the magnetic permeability of vacuum.

To draw a rudimentary picture of how light interact with molecules, the Lorentz model will be considered in this thesis. When looking at a dielectric material, in the presence of an electromagnetic wave of frequency ω, polarized in the x direction, the electrons are each subject to a driving force [1]:

$$\vec{F}_{driving} = q\,\vec{E} = q\,\vec{E}_0 \cos(\omega t)$$

[1]The level of transparency is dependent on the frequency of the electro-magnetic wave.

where q is electron charge and E_0 is the amplitude of the wave, and the electrons are bound to specific molecules. Since this system is being approximated as an harmonic oscillator, the binding force between the molecule and electron is considered to be represented by:

$$\vec{F}_{binding} = -m\omega_0^2\vec{x}$$

where x is the displacement from equilibrium, m is the electron's mass and ω_0 is the natural oscillation frequency. Further, there is an assumed damping force on the electrons:

$$\vec{F}_{damping} = -m\gamma\frac{d\vec{x}}{dt}.$$

Thus, according to Newton's 2nd law:

$$m\frac{d^2\vec{x}}{dt^2} = \vec{F}_{tot} = \vec{F}_{binding} + \vec{F}_{damping} + \vec{F}_{driving}.$$

From this the complex dipole moment can be derived [1]:

$$\tilde{p}(t) = q\tilde{x}(t) = \frac{q^2/m}{\omega_0^2 - \omega^2 - i\gamma\omega}E_0e^{-i\omega t}.$$

If it is assumed that there are f_j electrons with frequency ω_j and damping γ_j in each molecule and there are N molecules per unit volume, then the polarization of the material is given by the real part of

$$\tilde{P} = \frac{N\,q^2}{m}\left(\sum_j \frac{f_j}{\omega_j^2 - \omega^2 - i\gamma_j\omega}\right)\tilde{E}. \tag{2.4.17}$$

It can be shown that $\tilde{P}$ is proportional to $\tilde{E}$, this proportionality has the following form [1]:

$$\tilde{P} = \epsilon_0\tilde{\chi_e}\tilde{E}. \tag{2.4.18}$$

where $\tilde{\chi_e}$ is known as the complex susceptibility of the material. From the proportionality between $\tilde{D}$ and $\tilde{E}$ the complex permittivity $\tilde{\epsilon} = \epsilon_0(1 + \tilde{\chi_e})$ can be derived and thus it can be shown that the complex dielectric constant $(\tilde{\epsilon_r} = \tilde{\epsilon}/\tilde{\epsilon}_0)$ is:

$$\tilde{\epsilon}_r = 1 + \frac{N\,q^2}{m\epsilon_0}\sum_j \frac{f_j}{\omega_j^2 - \omega^2 - i\gamma_j\omega} \tag{2.4.19}$$

It can be seen that a complex nature arises in these equations. This is due to the dipole moment being out of phase with E. Accordingly it is found that the wave traveling through the media becomes [1]:

$$\widetilde{E}(z,t) = \widetilde{E}_0e^{-\alpha/2\,z}e^{i(kz-\omega t)} \tag{2.4.20}$$

where α is the absorption coefficient and k is known as the wave number. Thus the wave becomes attenuated [1]. This is the origin of the well known Beer-Lambert law.

2.5 Index of refraction

As previously mentioned, the index of refraction is given by $n = \sqrt{\frac{\epsilon\mu}{\epsilon_0\mu_0}}$. This can then also be interpreted as:

$$n = \frac{c}{v}. \tag{2.5.1}$$

Consequently, the index of refraction can be seen as the ratio by which light slows when moving through a certain material. The index of refraction can usually be approximated as $n \approx \sqrt{\epsilon_r}$, since usually $\mu \approx \mu_0$. Now, it should be noted that the wave velocity can be represented as follows $v = \omega/k$, thus accordingly the refractive index can be represented as:

$$n = \frac{ck}{\omega}. \tag{2.5.2}$$

Since n is closely related to ϵ_r ($n \approx \sqrt{\epsilon_r}$) and ϵ_r is complex and frequency dependent, it can be seen that n should also have these dependencies. These dependencies manifests as follows:

$$\widetilde{n}(\omega) = n(\omega) + iK(\omega) \tag{2.5.3}$$

$$K(\omega) = \frac{c\alpha(\omega)}{2\omega} \tag{2.5.4}$$

where K is known as the extinction coefficient and α is the absorption coefficient. $\widetilde{n}$ is known as the complex refractive index. A plot of the two components of the complex refractive index can be seen in figure 2.1 [1].

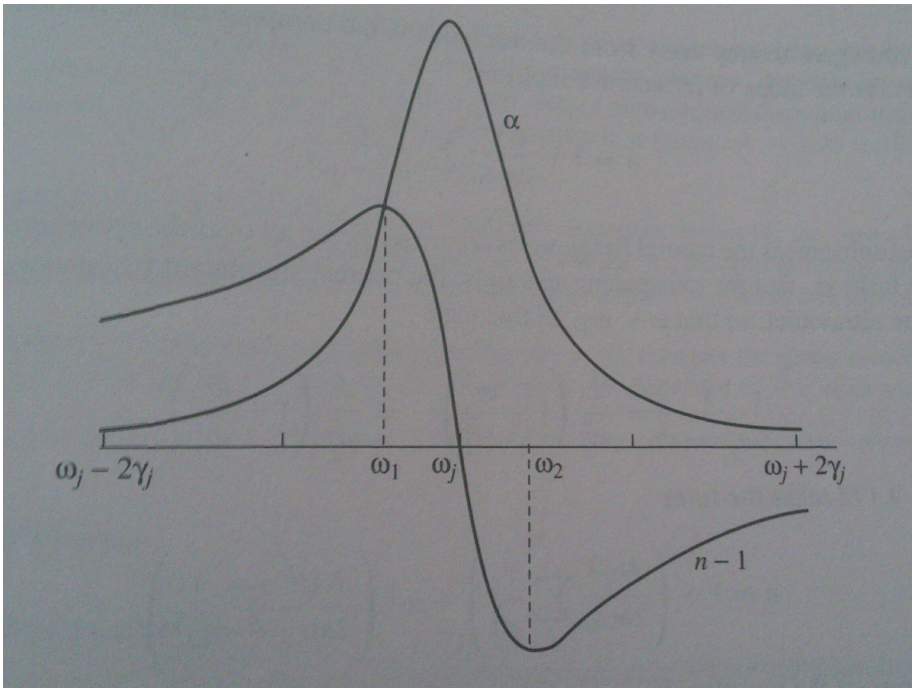

Figure 2.1: Absorption coefficient and refractive index near a resonance frequency, as represented by Griffiths et al [1].

2.6 Kramers-Kronig dispersion relations

As discussed in section 2.5, the refractive index is a complex, frequency dependent function. In order to extract this information from measured data, certain mathematical tools are needed. The Kramers-Kronig relations form a part of these tools.

According to the Kramers-Kronig relations it is possible to write a complex response function in terms of its real and complex components [10]:

$$\widetilde{X} = X_1(\omega) + iX_2(\omega) \tag{2.6.1}$$

where:

$$X_1(\omega) = \frac{1}{\pi} P \int_{-\infty}^{\infty} \frac{X_2(\omega')}{\omega' - \omega} d\omega' \tag{2.6.2}$$

$$X_2(\omega) = \frac{-1}{\pi} P \int_{-\infty}^{\infty} \frac{X_1(\omega')}{\omega' - \omega} d\omega' \tag{2.6.3}$$

where P denotes the Cauchy principal value and Ω is the frequency space.

The complex refractive index ($\widetilde{n}(\omega) = n(\omega) + iK(\omega)$) can be viewed as a complex response function and as such it is possible to use these relations to derive expressions representing its real and imaginary parts [11]:

$$n(\omega) - 1 = \frac{c}{\pi} P \int_0^\infty \frac{\Omega \alpha(\Omega)}{\Omega^2 - \omega^2} d\Omega \tag{2.6.4}$$

$$K(\omega) = \frac{c\alpha}{2\omega} = \frac{-2\omega}{\pi} P \int_0^\infty \frac{n(\Omega)}{\Omega^2 - \omega^2} d\Omega. \tag{2.6.5}$$

Using these relations, it is possible to extract the refractive index from absorption spectra and vice versa. This in turn offers in part a method for extracting the frequency dependent complex refractive index for materials from absorption spectra.

2.7 Extraction of the complex refractive index

Assume that the electric field traveling in the system is given by:

$$\widetilde{E} = E_0 e^{-i(\widetilde{k}(\omega)z - \omega t)} \tag{2.7.1}$$

where $\widetilde{k}(\omega)$ is the complex frequency dependent wavenumber and E_0 is the electric field amplitude. $\widetilde{k}(\omega)$ is related to the complex refractive index by:

$$\widetilde{k}(\omega) = \frac{\omega}{c} \widetilde{n}. \tag{2.7.2}$$

Now assume that a sample of thickness δz is introduced. If the origin of the z-axis is placed in front of the sample, then the electric field before the sample is given by:

$$\widetilde{E}(z = 0) = E_0 e^{i\omega t} \tag{2.7.3}$$

and after the sample, where $z = \delta z$, it will be:

$$\widetilde{E} = E_0 e^{-i(\widetilde{k}(\omega)\delta z - \omega t)}. \tag{2.7.4}$$

Thus $e^{-i(\widetilde{k}(\omega)\delta z)}$ represents the change in the electric field introduced by the sample.

In vacuum:

$$\widetilde{k}_{ref}(\omega) = \frac{\omega}{c}. \tag{2.7.5}$$

According to Lewis *et al.* [12], with a sample present it can be shown that:

$$\widetilde{k}_{sample}(\omega) = \frac{\omega}{c} + \frac{\omega}{c}[n(\omega) - 1] + i\frac{\alpha(\omega)}{2}. \tag{2.7.6}$$

Thus, the electric field after the sample will be given by:

$$\widetilde{E}(\delta z)_{sample} = E(z = 0) e^{-i(\widetilde{k}_{sample}(\omega)\delta z)}. \tag{2.7.7}$$

Without the sample present, the electric field at the same position will be given by:

$$\widetilde{E}(\delta z)_{ref} = E(z=0)e^{-i(\widetilde{k}_{ref}(\omega)\delta z)}. \tag{2.7.8}$$

The ratio between these two electric fields is given by:

$$\frac{\widetilde{E}(\delta z)_{sample}}{\widetilde{E}(\delta z)_{ref}} = e^{-i(\frac{\omega}{c}[n(\omega)-1]+i\frac{\alpha(\omega)}{2})\delta z} \tag{2.7.9}$$

$$= e^{-i\frac{\omega\,\delta z}{c}[n(\omega)-1]}e^{\frac{\alpha(\omega)\,\delta z}{2}} \tag{2.7.10}$$

$$\alpha(\omega) = \frac{2}{\delta z}\mathrm{Re}\left[\ln\frac{\widetilde{E}(\delta z)_{sample}}{\widetilde{E}(\delta z)_{ref}}\right] \tag{2.7.11}$$

$$n(\omega) = \frac{c}{\omega\,\delta z}\mathrm{Im}\left[\ln\frac{\widetilde{E}(\delta z)_{ref}}{\widetilde{E}(\delta z)_{sample}}\right] + 1. \tag{2.7.12}$$

In these equations one finds that the absorption coefficient is given by the real component of the exponential and the refractive index is given by the complex components. Thus the absorption coefficient can be calculated from the frequency based amplitude ratio of a measurement with and without a sample present. Similarly the refractive index can be calculated from the ratio between the two sets of phase data. These calculated values can then be verified using the Kramers-Kronig relations [12].

2.8 The Drude model

In this chapter the Drude model will be discussed. This model is used to explain the electron behavior of solid state materials and can be of use for more in depth analysis of measured data.

The Drude model is a statistical model, with which the electron nature of metals can be modeled. In this model, the kinetic gas model is applied to metals by approaching them as a gas of electrons. Unlike a gas of electrons though, a metal consists of two types of particles, not just one, since they have a neutral net-charge. The first type of particle is the electron and the second is considered to be a far heavier, positively charged particle which stays immobile. In this system, there are two types of electrons, namely valence electrons and core electrons. Valence electrons are considered to be detached from their atom and can move freely in the metal, while the core electrons form closed shells in the atomic structure and remain bound to their atoms.

In the Drude model a few assumptions are made when it comes to treating how particles in the system interact with one another. The only interactions considered in this model are collisions (both electron-electron and electron-ion collisions are considered), all other interactions between particles are ignored,

such as with the potentials and fields generated by the particles. Accordingly, in the absence of an externally applied electric field, the electrons will move in a straight line until they experience a collision. If an external electric field is applied to the system, the electrons will move in accordance with Newton's laws of motion. When an electron experiences a collision, it occurs instantaneously and abruptly alters the velocity of the electron. The rate at which these collisions occur is given by $\frac{1}{\tau}$, where τ is seen as the relaxation time of the material and is independent of both the momentum and position of the electron. When an electron collides it is "thermalized", which means that it is given a velocity with a random direction and a speed that is determined by the temperature of the system, this process is independent of the velocity of the electron prior to the collision. Via this "thermalization" process the system is allowed to reach thermal equilibrium.

This model can be used to describe both electrical and thermal conductivity in metals. Since semiconductors behave similar to metals when excited, this can be used as a tool to help analyze data taken from excited semiconductor samples [13]. This model can potentially be useful when analyzing terahertz time-domain spectroscopy data from semiconductor samples.

Chapter 3

Terahertz generation and detection

In this chapter, two methods of terahertz generation and detection will be discussed. Currently these two methods are the most widely used for in-lab broadband terahertz spectroscopy and thus are the most relevant options to this thesis.

3.1 Terahertz generation

Currently a few methods of coherently generating terahertz radiation exist. In the optical world four main methods are currently employed: optical rectification via either electro-optical crystals (EO crystals) or plasmas, quantum cascade lasers and photoconductive antennae (PC antennae). Two of these methods will be discussed in this chapter, namely optical rectification via EO crystals and photoconductive antennae. Photoconductive antennae will be used in the setup discussed in this thesis.

3.1.1 Optical rectification

Terahertz generation in EO crystals is done via a second order nonlinear process known as optical rectification. Optical rectification is second order difference frequency generation. A diagrammatic representation of difference frequency generation can be seen in figure 3.1. The one component in this effect is approximated as the square of the envelope of the electric field of the incident electric field, since the frequency components of the carrier wave are much higher than those of the envelope of the optical pulse. This allows the generation of pulses in the terahertz regime. Since this is just a second order optical effect, the generated terahertz pulse has an electric field amplitude that is proportional to the intensity of the incident pump pulse. Similarly, the temporal width of the generated pulse also depends on the temporal width of

the pump pulse.

$$P(\omega) = \epsilon_0 \chi^{(2)} \int_{-\infty}^{\infty} E(\omega') E^*(\omega' - \omega) d\omega' \tag{3.1.1}$$

$$P(t) = \epsilon_0 \chi^{(2)} E(t) E^*(t) \tag{3.1.2}$$

where P is the second order polarization induced by the incident pump pulse, $\chi^{(2)}$ is the second order susceptibility of the material, E is the electric field of the pump pulse. From Maxwell's equations it can be shown that [14]:

$$E_{THz}(t) \propto \frac{\partial^2 P(t)}{\partial t^2} \tag{3.1.3}$$

where E_{THz} is the electric field of the generated terahertz pulse. These equations make use of the plane-wave approximation. From Fourier theory (equation C.0.8 in appendix C) it can be shown that this implies that there is a direct relation between the bandwidth of the optical pump pulse and the bandwidth of the generated terahertz pulse.

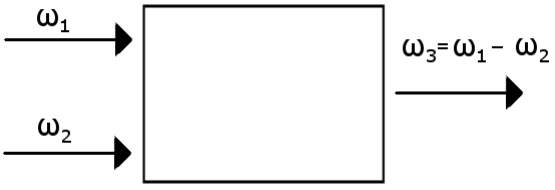

Figure 3.1: Diagram representing difference frequency generation

Consequently, if a Gaussian temporal pulse is used to pump the EO crystal, a Gaussian temporal terahertz pulse should be generated. Theoretically, some EO crystals should be able to generate pulses with a bandwidth of up to 100 THz (an example of such a pulse can be seen in the work done by A. Brodschel *et al.* as is displayed in figure 3.2 [2]), and the main limiting factor in the system is the pump laser. Examples of materials used as EO crystals are ZnTe and GaP [7].

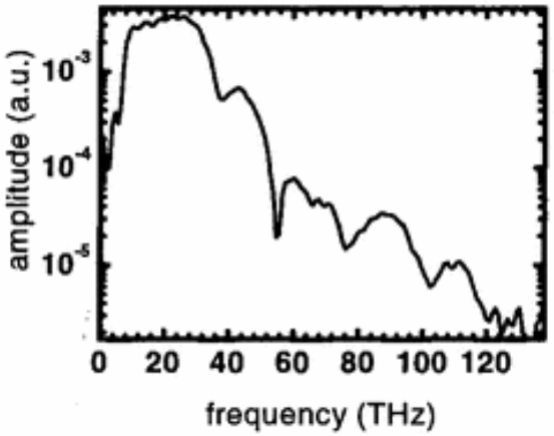

Figure 3.2: The measured amplitude spectrum of the transient emitted via optical rectification. A 20 μm thick GaSe crystal was used as the nonlinear medium and a 10.3 μm ZnTe Electro-optical crystal was used as the detector. This measurement was performed by A. Brodschel *et al.* [2]

3.1.2 Photoconductive antennae

A photoconductive antenna is a Hertzian styled dipole antenna, except that instead of a conventional resistor a semiconductor material which can be photo excited into a conducting state is used. A schematic of an photoconductive antenna can be seen in figure 3.3. How this works is that the material in question has a large resistance, and thus has no electrons in the conduction band when it is in the ground state. By using light with photon energy higher than the bandgap it is possible to excite valence electrons into the conduction band, thus transforming the material into a conductor. These electrons will then de-excite over time and the material will return to an insulating state. The speed at which these electrons become de-excited on average is a characteristic of the material, which is known as the excitation life-time. In the case of the terahertz photoconductive antenna, this material acts as a switch. To achieve this functionality the photoconductive material used needs certain characteristics: when in its ground state the material should be a very strong insulator, so that the circuit will essentially be open. When excited the material should be a very good conductor, so that the circuit will in essence be an LC-circuit. Lastly, the material needs to have a very short excitation life-time, so as to achieve short terahertz pulses. Radiation damaged silicon on sapphire, Cr doped GaAs and low temperature grown GaAs are materials commonly used photoconductive materials.

The setup employed in this thesis makes use of photoconductive antennae. The PC antennae in this setup uses low temperature grown GaAs (LT-GaAs),

which has an excitation life-time of 300 fs, moderate conductivity when excited and is a good insulator when in the ground state [7].

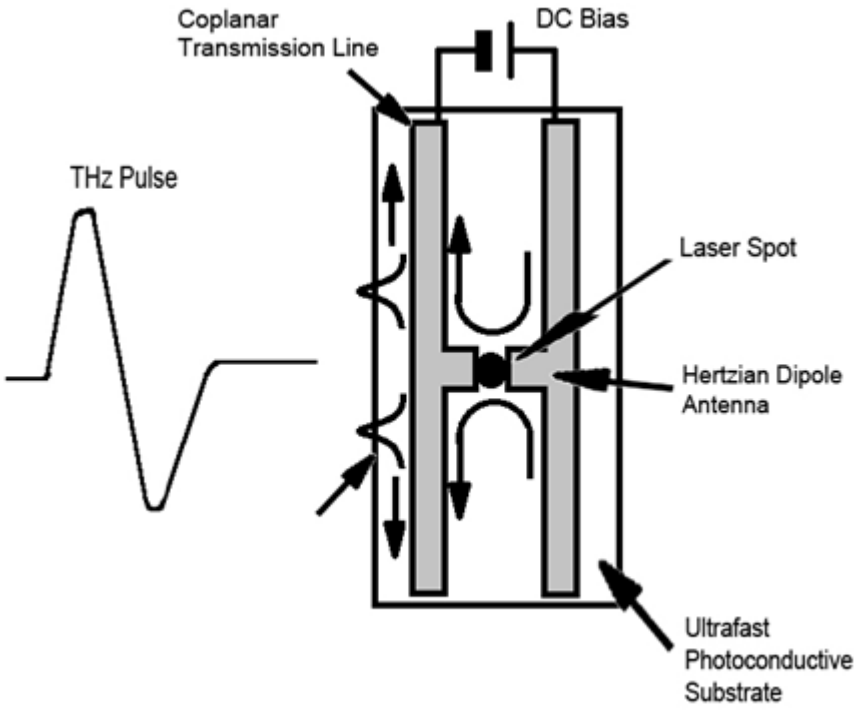

Figure 3.3: Schematic of a photoconductive antenna.

The electric field generated by the antenna, when the photoconductive substrate is excited, can be described by the following equation:

$$E(r,t) = \frac{l_e}{4\pi\epsilon_0 c^2 r}\frac{\partial J(t)}{\partial t}\sin\theta \tag{3.1.4}$$

where $J(t)$ is the current in the dipole, l_e the effective length of the dipole and θ the polar observation angle for the dipole [7].
In the system in use, θ is taken to be 90°, since the emitter and detector are parallel to one another, and l_e is a constant (l_e is taken to be equal to the electrode separation gap size) and r is the distance between the emitting and receiving antennae (35 cm in the setup constructed during this thesis) [7].

The current in the dipole is dependent on a few factors and can be calculated as follows:

$$J(t) = \int I_{opt}(t-t')[\mathrm{e}\, n_c(t')\, v(t')]dt' \tag{3.1.5}$$

where $I_{opt}(t)$ is the intensity profile of the optical pump pulse, e is the charge of an electron, $n_c(t)$ is the carrier density and $v(t)$ is the average electron velocity

[15]. According to Lee *et al.* [15] it can be shown that:

$$n_c(t) = \begin{cases} e^{-t/\tau_c} & \text{for } t > 0 \\ 0 & \text{for } t < 0 \end{cases} \tag{3.1.6}$$

and

$$v(t) = \begin{cases} E_{DC}\frac{e\tau_s}{m}[1 - e^{-t/\tau_s}] & \text{for } t > 0 \\ 0 & \text{for } t < 0 \end{cases} \tag{3.1.7}$$

where τ_c is the carrier lifetime (200 fs for LT-GaAs), τ_s is the momentum relaxation time ($20 - 30$ fs for LT-GaAs), m is the effective mass of the charge carriers and E_{DC} is the applied bias field. If the pump pulse is taken to be Gaussian and has a pulse duration of $2\sqrt{\ln 2}\tau_p$ and has an intensity of I^0_{opt}, equation 3.1.5 can be written as [15]:

$$J(t) = \frac{e\tau_s}{m} E_{DC} I^0_{opt} \int_0^\infty e^{-(t-t')^2/\tau_p^2 - t'/\tau_c}[1 - e^{-t'/\tau_s}]dt'. \tag{3.1.8}$$

Thus, it can be seen that the produced terahertz electric field will be dependent on both the relaxation times of the photoconductive material and the pulse duration of the optical pump pulse.

These antennae allow for moderately large bandwidths[1] without the need of extremely short pulsed lasers[2], thus reducing the cost of the equipment needed for the setup. These antennae are also less expensive to manufacture than EO crystals. The main shortcomings of PC antennae as terahertz source is that they are rather intensity limited when compared to the other methods.

3.2 Terahertz detection

In this section two of the most common methods of terahertz detection will be discussed, electro-optical sampling and detection via PC antennae.

3.2.1 Electro-optical sampling

This is a phase sensitive detection method based around the birefringent nature of EO crystals. The incident terahertz radiation causes the EO crystal to become birefringent due to the Pockels effect [7]. A probe pulse is then sent through the crystal and the induced birefringence is measured as a phase-shift between the parallel and perpendicular polarization components of the probe pulse. The EO crystal is nonresonant for the probe pulse, which allows for instantaneous sensing of the induced birefringence. This method of terahertz

[1] About 4 THz

[2] a femtosecond laser with a pulse duration of 87.8 fs was made use of in this thesis

detection allows for broad bandwidth detection[3] due to its nonresonant nature. The phase retardation in the crystal is represented by the following equation:

$$\Delta\Gamma(t) = \frac{2\pi}{\lambda} d n_{opt}^3 r_{41} E_{THz}(t) \tag{3.2.1}$$

where d is the EO crystal thickness, n_{opt} is the group refractive index of the EO crystal at the wavelength of the near-infrared probe pulse and r_{41} is the electro-optical coefficient [7].

3.2.2 Photoconductive antennae

Detection of terahertz pulses via photoconductive antennae is quite similar to how terahertz pulses are generated via photoconductive antennae, except that instead of a bias current being applied to the antenna, the incoming terahertz pulse accelerates the charge carriers that have been excited into the conduction band by the optical pump pulse, thus generating a current, which can then be measured. The induced current can be represented as follows:

$$J(t) = \mathrm{e}\mu \int_{-\infty}^{\infty} E(t') N(t' - t) dt' \tag{3.2.2}$$

where $E(t')$ is the incident electric field, $N(t')$ is the number of photo created charge carriers, e is the elementary electric charge and μ is the electron mobility. From this, it can be found that the current generated will only represent a small gated part of the terahertz pulse and, accordingly, multiple measurements with different temporal shifts need to be taken in order to measure the entire pulse. In order to take measurements of the pulse, a delay line is used to synchronize the arrival of the optical pump pulse with that of the terahertz pulse at the receiving antenna in time. This delay line is then used to alter the arrival time of the terahertz pulse, while keeping the arrival time of the optical pulse constant. In doing so, it is possible to measure different sections of the terahertz pulse in time. Accordingly, the main component to determine the temporal resolution of the measurement is the step size employed by the delay line [7].

One of the limiting factors for detection via photoconductive antennae is that the photoconductive substrate used in the antenna can have terahertz resonances at certain of the frequencies contained in the terahertz pulse. This is the case for LT-GaAs, which has an absorption band between $5 - 10\,\mathrm{THz}$, making it poorly suited to larger bandwidth measurements.

[3] $> 5\,\mathrm{THz}$ bandwidth is possible

Chapter 4

Experimental setup

In this chapter the setup used during this thesis will be discussed. This includes the discussion of key elements in its operation and the alignment of the setup.

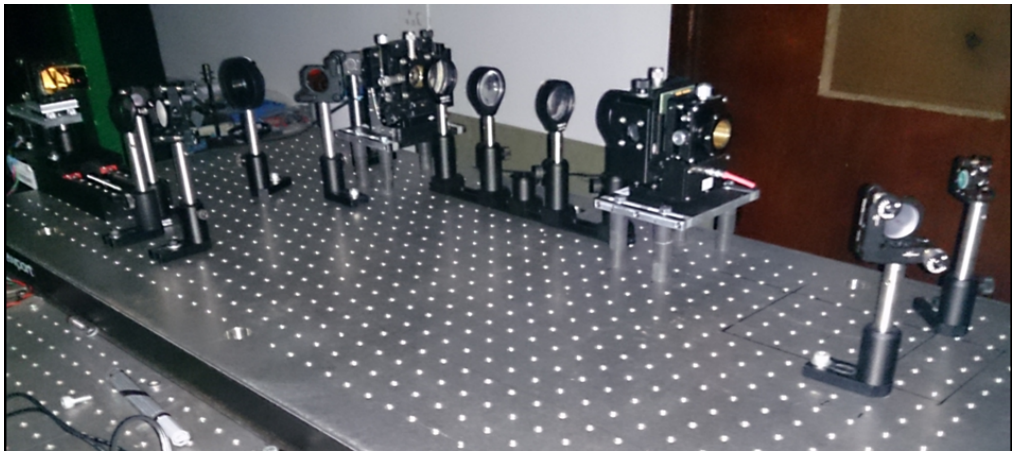

Figure 4.1: Photo of the setup constructed and used in this thesis.

4.1 Setup

The system mainly consists of four components: two photoconductive antennae, a translation stage with a retro-reflector mounted on it and a femtosecond laser.

Using a beam splitter, the pulse from the femtosecond laser is divided with half of the pulse going to the one photoconductive antenna, which has a voltage applied across it, exciting the resistor and allowing the circuit to oscillate, thus inducing the generation of electric dipole radiation. The other part of the pulse is sent to a translation stage. From there it is reflected to the receiving antenna, but this second antenna does not have a potential applied

to it. Instead the antenna receives the incoming radiation from the emitting antenna. The incoming terahertz electric field then accelerates electrons in the circuit, thus producing a current, which can then be measured.

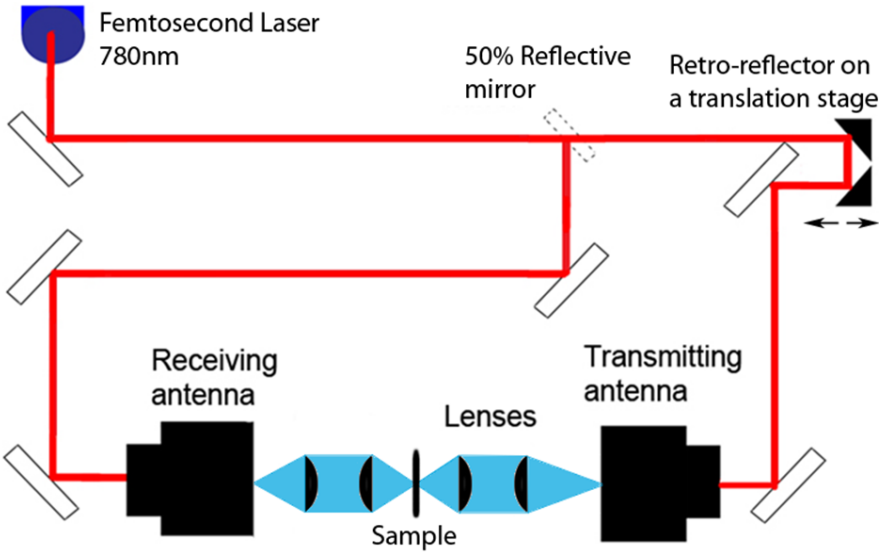

Figure 4.2: Diagram of a terahertz time-domain transmission setup as constructed for this thesis.

The translation stage is then used to change the time at which a part of the pulse is measured, by changing the distance the light from the laser has to travel to the transmitting antenna (it should be noted that a current can only be measured while the resistor is in a conducting state). Thus a lot of small measurements are taken of the pulse at different times.

Each point on the translation stage where a measurement was performed represents a single data point of the pulse. Thus, by plotting all the data points, an image of the pulse is produced.

In the setup built for this thesis an amplified voltage of $\approx$ 22 V, with a $\approx$ 1 kHz repetition rate, was used to drive the transmitting antenna. A measurement of this voltage can be seen in figure 4.3.

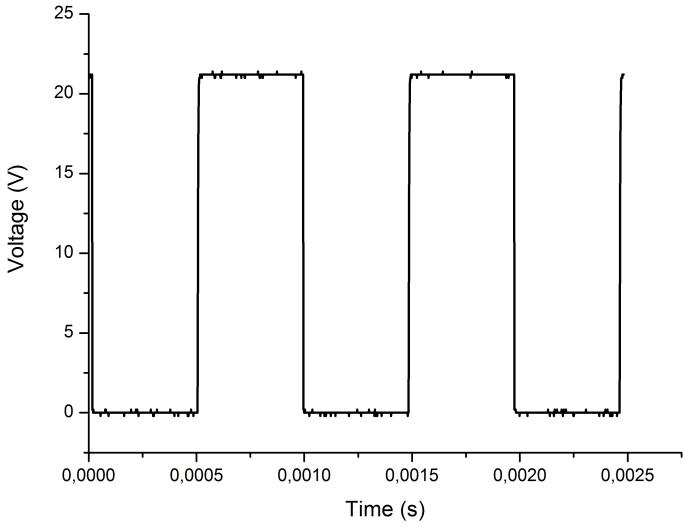

Figure 4.3: Voltage applied to the emitting antenna. A modulated current is used to ease the use of the lock-in amplifier.

4.2 Femtosecond laser

A titanium-sapphire based femtosecond laser is implemented as the pump source for the antennae in the setup used in this thesis. In this chapter the laser used in the setup will be briefly discussed.

Callout	Description
1	Beamsplitters 1 through 4
2	Output coupler
3	Slit
4	Flat cavity mirror
5	Starter
6	Birefringent filter
7	Titanium:sapphire crystal
8	Flat cavity mirror
9	Lens 1
10	Brewster prism 2
11	Flat mirror
12	Laser head interface panel
13	Pump fold mirror
14	Pump optics 1 through 4
15	Flat end mirror
16	Flat mirror (auxiliary cavity)
17	Brewster prism 1
18	Curved mirror
19	Cooling water lines
20	Curved mirror
21	Cavity length control
22	Auxiliary cavity end mirror
23	Head board

Table 4.1: List of femtosecond laser components.

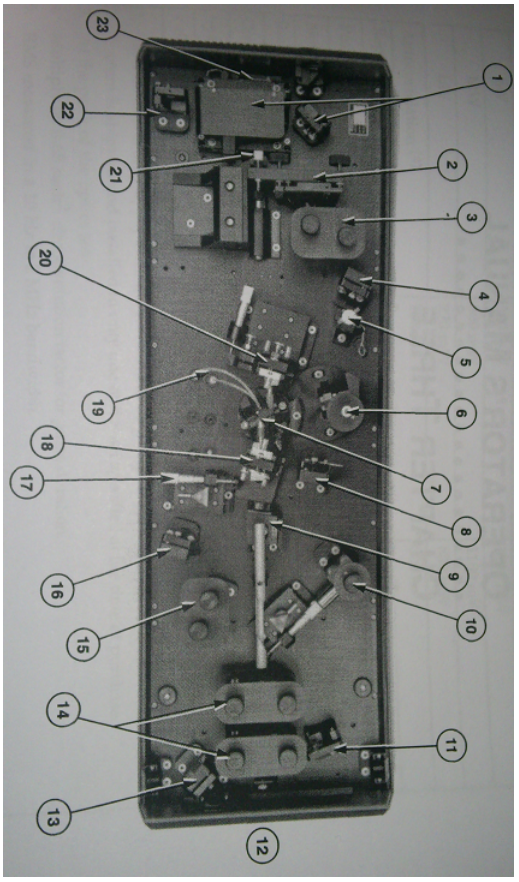

Figure 4.4: Diagram of femtosecond laser used in the system.

In order to generate ultrashort laser pulses, as is needed for gating the antennae in this system, conventional cavity based lasing techniques can not be employed due to the restrictions of cavity dynamics. Instead, a technique known as mode-locking is made use of. In a cavity, all modes with higher gains than losses will propagate. If these modes have the same phase, they will constructively interfere with one another. If enough such modes interfere with one another, the resultant interference will be a broad spectrum pulse. From Fourier analysis, it can be shown that the broader a pulse's spectrum is, the shorter its duration can be. Mode-locking refers to techniques used to induce this phase equality into a multi-mode system [16].

The laser used in this thesis makes use of a technique known as self-locking. The laser achieves femtosecond pulses through the Kerr effect. This is a non-linear effect that introduces an intensity dependence to the refractive index of

the amplification medium:

$$n = n_0 + n_2 I(t). \tag{4.2.1}$$

This effect is related to the Kerr lens effect, thus also introducing self-focusing into the medium. This self-focusing also strongly favours higher intensities, thus modes with higher intensities will be more focused than modes with lower intensities. But this in turn would mean that under normal circumstances the continuous wave beam in the cavity would dominate. A rapidly oscillating optical slide (Figure 4.4 number (5)) is thus used to temporarily block all modes in the laser cavity and allow the mode with the least loses to dominate. Introducing a slit of the right size (Figure 4.4 number (3)) greatly aids this effect by adding losses to the continuous wave mode, while not doing so for the pulsed mode, due to the self focusing which will focus the pulsed light much more than the continuous wave, thus the pulsed mode will be smaller than the continues wave mode. Accordingly, the introduction of such a slit will help prevent the continuous wave mode from becoming dominant again after the starting process [16].

Normally as the pulse travels in the laser cavity, it experiences an effect known as dispersion. This comes from the refractive index being frequency dependent. If the different frequency components of the pulse move through materials where they experience different refractive indices, such as in the gain medium, then they will experience different phase shifts, which will undo the mode-locking of the pulse, accordingly this needs to be compensated for. In the cavity dispersion is compensated for by making use of two prisms (Figure 4.4 number (10) and (17)). When making use of prisms for this purpose, their position in the beam can be optimized to maximize the bandwidth [16].

A birefringent filter is used in the cavity to choose the central wavelength of the pulse.

The two prisms used in the cavity for dispersion compensation are inserted at the Brewster angle. According to the Fresnel equations this will introduce an extra loss to light polarized perpendicular to the plane of incidence, while not doing so for parallel polarized light. This might at first be a small difference that is introduced between the two polarizations, but due to the nature of the laser this will ultimately lead to the one polarization heavily dominating over the other and the resultant pulse will be polarized [16].

To illustrate how large the impact of mode-locking is on the bandwidth of the laser, spectral measurements of the output from the femtosecond laser source used in this thesis were taken before and after mode-locking. The continues wave mode can be seen in figure 4.5 and the pulsed mode can be seen in figure 4.6.

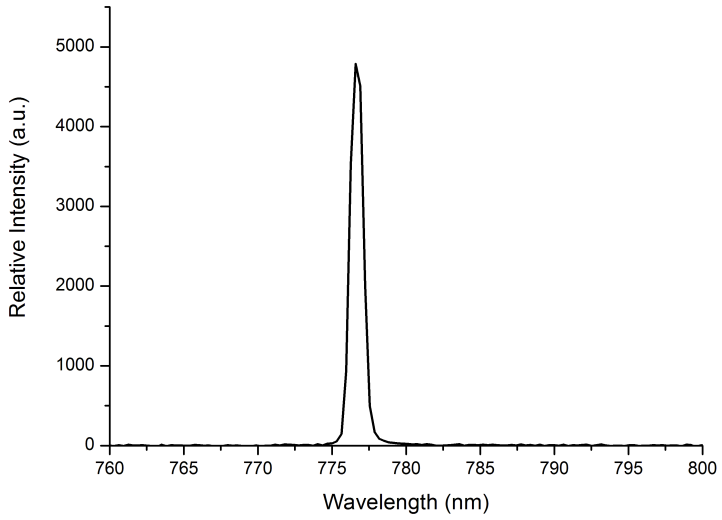

Figure 4.5: The spectrum of the pulse before it has been mode-locked as measured by the spectrometer. The spectrum has a FWHM of 1.06 nm.

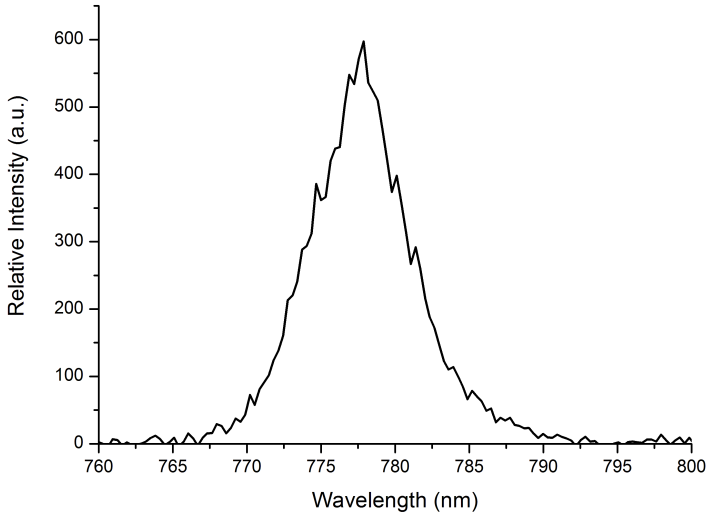

Figure 4.6: The spectrum of the pulse once it has been mode-locked as measured by the spectrometer. Broadening of the bandwidth is clearly visible. The spectrum has a FWHM of 7.81 nm.

4.3 Autocorrelator

Due to their short duration and the speed limitations of photo-detectors, the pulse duration of femtosecond pulses can not be measured electronically. Thus, in order to measure the durations of these pulses, optical methods must be used. These methods make use of non-linear optical effects to measure the pulse duration. For this thesis a method known as interferometric autocorrelation was made use of.

4.3.1 Interferometric autocorrelator

In an interferometric autocorrelator a femtosecond laser pulse is made to interfere with a copy of itself in a non-linear medium. The non-linear process that is being considered in this case is two photon absorption. To do this, the pulse is split in two. As the two pulses overlap with one another in both space and time in the non-linear medium, the signal produced by the two photon absorption process greatly increases, since the process scales with intensity squared. The greater the degree of temporal overlap, the greater the intensity of the two photon absorption process. It should be noted that the detector is not sensitive to one photon absorption, due to a single photon not having enough energy to excite an electron across the bandgap of the material employed in the detector. The detector used in this autocorrelator is a GaAlAs LED, this this LED operates at 660 nm and has a bandwidth of 20 nm.

For the autocorrelator used in this thesis a Michelson interferometer based design was used. The one arm to which the light was reflected had a fixed mirror, while the other path had a movable mirror[1]. By making use of the movable mirror, the degree of temporal overlap can be altered while keeping the spacial overlap constant, resulting in varying constructive and destructive interference.

[1]The mirror was moved using a shaker device. The shaker used in this setup was a speaker which was attached to a signal generator. The signal generator was set to deliver a sinusoidal wave with a frequency of 16 Hz and an amplitude of 4 V

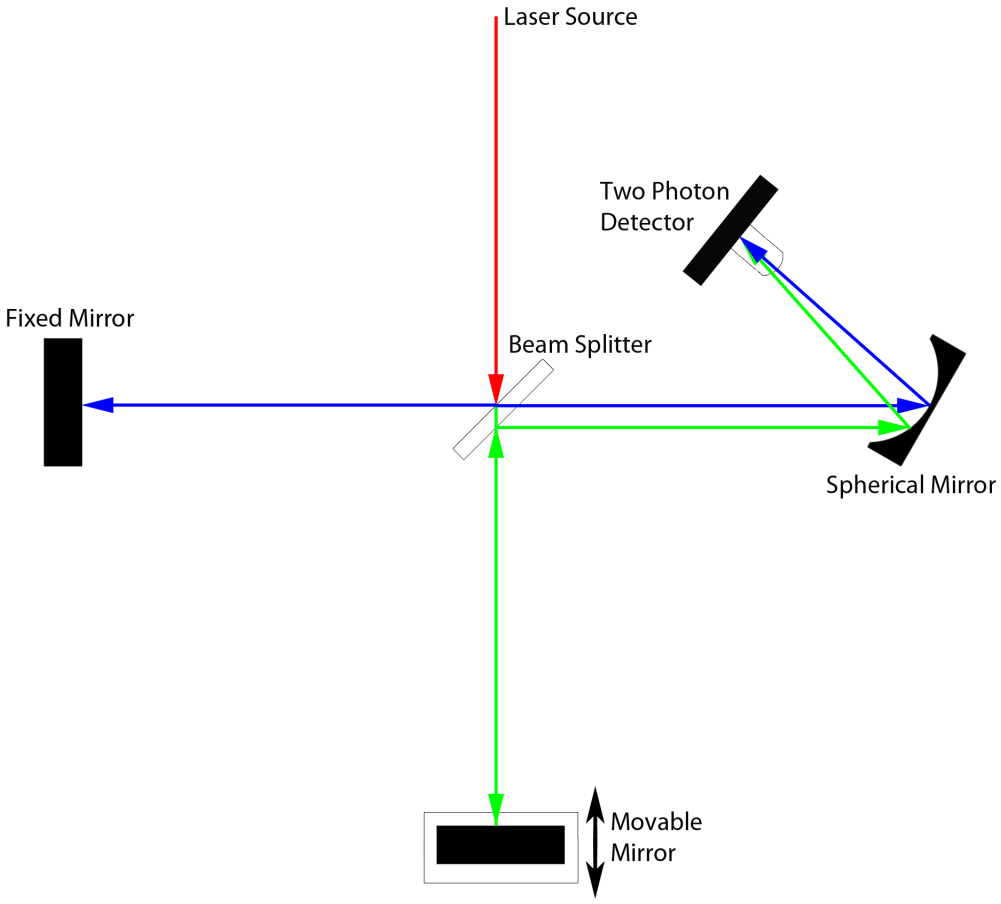

Figure 4.7: Schematic of an interferometric autocorrelator.

If it is assumed that the femtosecond pulse has a Gaussian temporal profile and is unchirped, the actual duration of the femtosecond pulse can be related to the interferogram measured via this method by use of the following equation:

$$I_{AC}(\tau) = \int_{-\infty}^{\infty} (|E(t) + E(t-\tau)|^2)^2 dt. \tag{4.3.1}$$

where I_{AC} is the envelope of the interference pattern generated, $E(t)$ is the electric field of the pulse and τ is the temporal difference introduced by the movable mirror. $|E(t) + E(t-\tau)|^2$ is used since the this process is intensity dependent, and this is then squared, since since this is a two photon absorption process.
The electric field is taken to be Gaussian:

$$E(t) = e^{\frac{-t^2}{w^2}}. \tag{4.3.2}$$

Thus for the used electric field it can be shown that:

$$w = \frac{FWHM_{pulse}}{\sqrt{2\ln(2)}} \tag{4.3.3}$$

and:

$$I_{AC}(\tau) = \sqrt{\pi}w(1 + 4e^{\frac{-3\tau^2}{4w^2}} + 3e^{\frac{-\tau^2}{w^2}}). \tag{4.3.4}$$

where FWHM is the width of the peak in time at half of its maximum value.

Accordingly the relationship can be shown between FWHM of applied electric field and the FWHM of the measured autocorrelator signal is given by:

$$FWHM_{pulse} = \sqrt{\frac{\ln(2)}{2}} FWHM_{AC}. \tag{4.3.5}$$

The full width at half-maximum is taken to be double the half width at half-maximum in these equations.

Since in this case it is taken that the Electric field is real, equation 4.3.1 can be rewritten as follows:

$$\begin{aligned} I_{AC}(\tau) = \int_{-\infty}^{\infty} \quad (\quad & E^4(t) + 4(E^2(t) + E^2(t-\tau))E(t)E(t-\tau) \\ + \quad & 6E^2(t)E^2(t-\tau) + E^4(t-\tau))dt. \end{aligned} \tag{4.3.6}$$

Where $E(t)E(t-\tau)$ is dependent on the overlap of the two electric fields (thus $\lim_{\tau\to\infty} E(t)E(t-\tau) = 0$) and, since the same electric field is used, just with a temporal shift, $E^4(t) = E^4(t-\tau)$. If it is taken that the two electric fields have a perfect overlap at $\tau = 0$, then it follows that:

$$I_{AC}(\tau = 0) = 16 \int_{-\infty}^{\infty} E^4(t)dt \tag{4.3.7}$$

$$I_{AC}(\tau \to \infty) = 2 \int_{-\infty}^{\infty} E^4(t)dt. \tag{4.3.8}$$

Accordingly, it is found that the interferometric autocorrelator has a maximum to background signal of $8:1$.

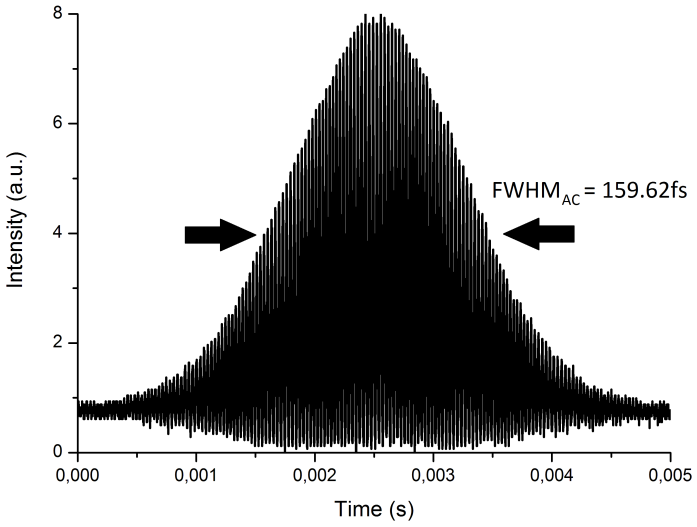

Figure 4.8: An interferogram measured by the autocorrelator constructed for this thesis. The measurement was taken with an oscilloscope and is calibrated in terms of the shaker's movement. The time scale is based on the oscillation speed of the shaker. The oscillated at 16 hz, and thus the oscilloscope was set to 20 ms per division.

This interferogram consists of many fringes. To relate this measurement to femtosecond scale, the fringes are each taken to be one wavelength apart. Using the speed of light to translate this value from distance to time, this interferogram can then be translated to femtosecond scale.

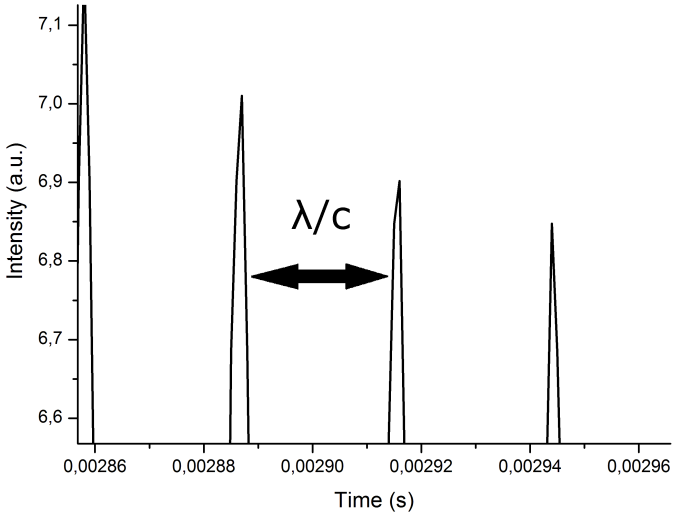

Figure 4.9: A zoomed in images of a section of fringes from figure 4.8. Each of these fringes is taken to be one wavelength apart.

In the case of this measurement, it was found that there are 61 fringes above half-maximum point. The central wavelength of the pulse was 785 nm, so accordingly it was found that the $FWHM_{AC} = 159.62$ fs, and thus the $FWHM_{pulse} = 93.4$ fs.

4.4 Power

To not degrade the antennae used in the system, their power threshold must not be exceeded by the beam with which the photoconductive substrate of the antennae is pumped.

The specifications received with the antennae were based around a pump source different from the one implemented in the setup used in this thesis. Accordingly specifications suited to the pump source in use needed to be calculated. Power can be viewed in two ways, peak power and average power. Where the peak power represents the power of a single pulse from the laser and average power is the average power of the pulse train.

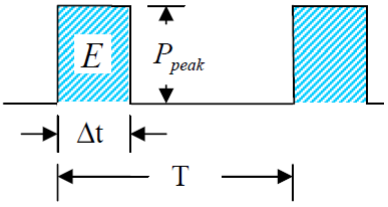

$$P_{peak} = \frac{E}{\Delta t} \tag{4.4.1}$$

$$P_{average} = \frac{E}{T} = Ef. \tag{4.4.2}$$

The peak power as calculated in accordance to the given specifications and the peak power applied must be the same, but what is given and usually measured is the average power. Actually, the peak intensity is what should be the same, but since the antennae are in the focus of a lens in both cases, it can be assumed that the beam spot size is the same on the antennae. And then, since $I_{peak} = \frac{P_{peak}}{Area}$ we can assume that the peak power should be the same in the two systems. Thus we must translate the average power for our system, which we can do via:

$$P_{Avg2} = P_{Avg1}\frac{f_2\Delta t_2}{f_1\Delta t_1}. \tag{4.4.3}$$

where f is the repetition rate of the pulse and Δt is the duration of the pulse. The average power listed in the antenna specifications is 10 mW, with a repetition rate of 100 MHz and a pulse duration of 94 fs. The pump laser used in this setup has a repetition rate of 80 MHz and a pulse duration of 93.4 fs. Thus the antenna should not be driven with more than 7.95 mW.

4.5 Lock-in amplifier

In this system, a lock-in amplifier is used as both the power source with which the emitting antenna is biased and as an amplifier to measure the current from the receiving antenna. Lock-in amplifiers are rather sophisticated pieces of equipment that can be used to amplify signals that repeat at a set rate.

The lock-in amplifier used in this system is a Stanford Research Systems SR830 DSP Lock-In Amplifier.

4.5.1 Setting up and testing

To test the settings on the lock-in amplifier, it was attached to a commercial setup with similar specifications to the setup constructed during this work. The bias voltage on the antenna was used as the reference signal. The data from the receiving antenna was monitored via an oscilloscope (Tektronix TDS 3032) attached to the output of the lock-in amplifier. To then be able to measure the pulse, a shaker[2], with a sinusoidal nature, was made use of to alter the part of the pulse which was measured in a repetitive fashion.

For the most part, three of the settings were focused on for the lock-in amplifier: The time constant, the slope and the sensitivity. The time constant is in a rough sense the slices of time over which the amplifier integrates the current which it receives. The slope is a measure by which the amplifier recognizes a signal from background noise or artifacts. The sensitivity sets the expected range in which the integrated voltage should be, and accordingly by how much the signal needs to be amplified.

The following settings were used:
Time Constant: 30 ms
Slope: 12 dB
Sensitivity: 50 μV

With these settings the data sets in figure 4.10 were produced:

[2] A shaker is a device that performs small, rapid, repetitive back and forth motions. This device is mounted on the translation stage and then a mirror is mounted onto it. The shaker is then moved via the translation stage to approximately where the pulse is expected to be, thus allowing for rapid measurements of the pulse. This comes at the cost of resolution, but is very useful when high resolution is not necessary such as during alignment.

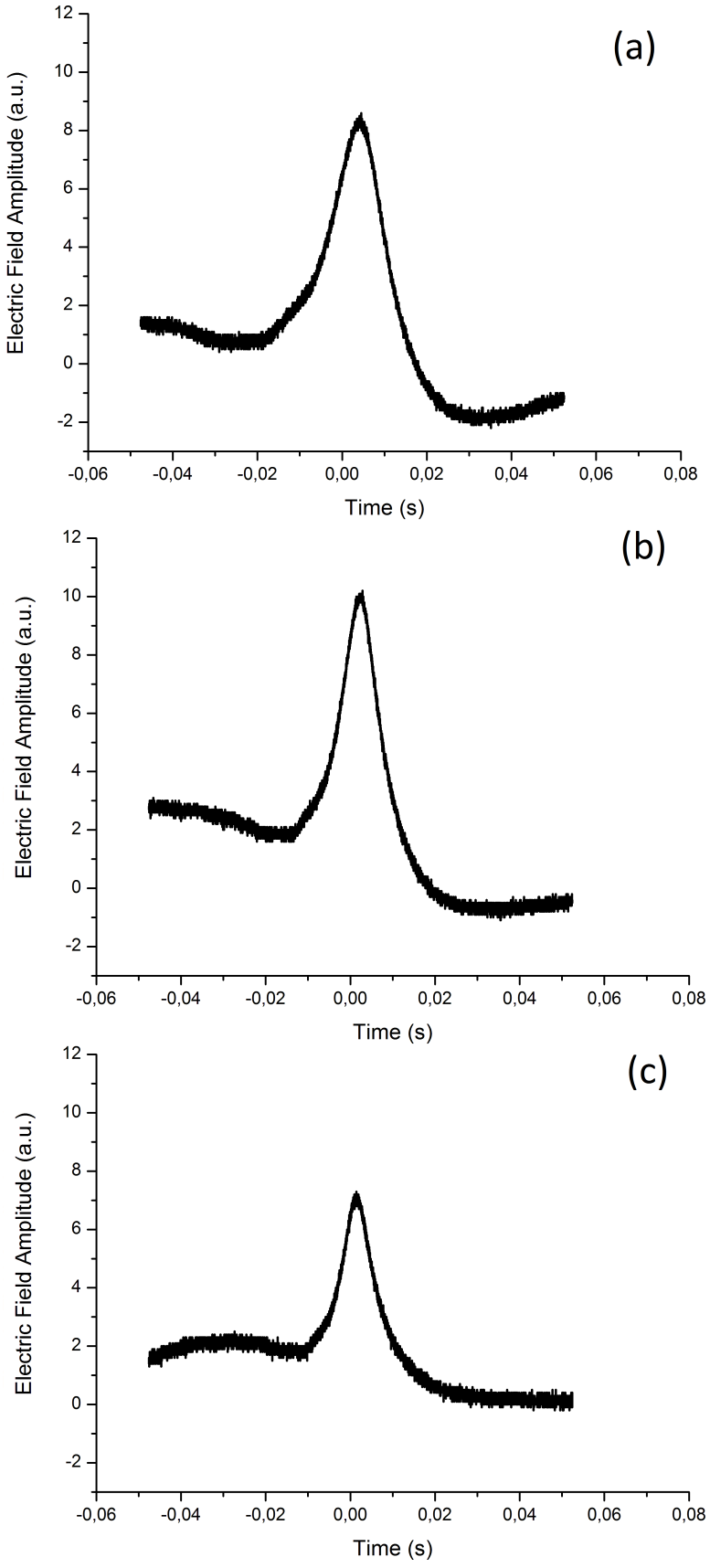

Figure 4.10: The electric field measured by the oscilloscope when the shaker was set to different frequencies. In (a) the shaker was set to 2 Hz, in (b) the shaker was set to 3 Hz and in (c) the shaker was set to 4 Hz. In all three cases an amplitude setting of 1.8 V was used.

In the third measurement the sensitivity was decreased to 100μV, due to its signal being too strong for the current setting, so it can't really be compared to the others

As can be seen, if the frequency of the shaker is increased, it results in a reduced amplitude for the resultant measurement. Setting the shaker to a higher frequency can sometimes be useful when a lot of low resolution measurements need to be taken, such as during imaging. In this case the reduction in time needed per scan might be worth the reduction in intensity.

For the next few measurements the shaker settings were kept constant and the time constant of the lock-in amplifier was altered, the sensitivity was then set so as to have maximal output and not overload the lock-in amplifier. The shaker's frequency was set to 3 Hz and its amplitude to 1.8 V.

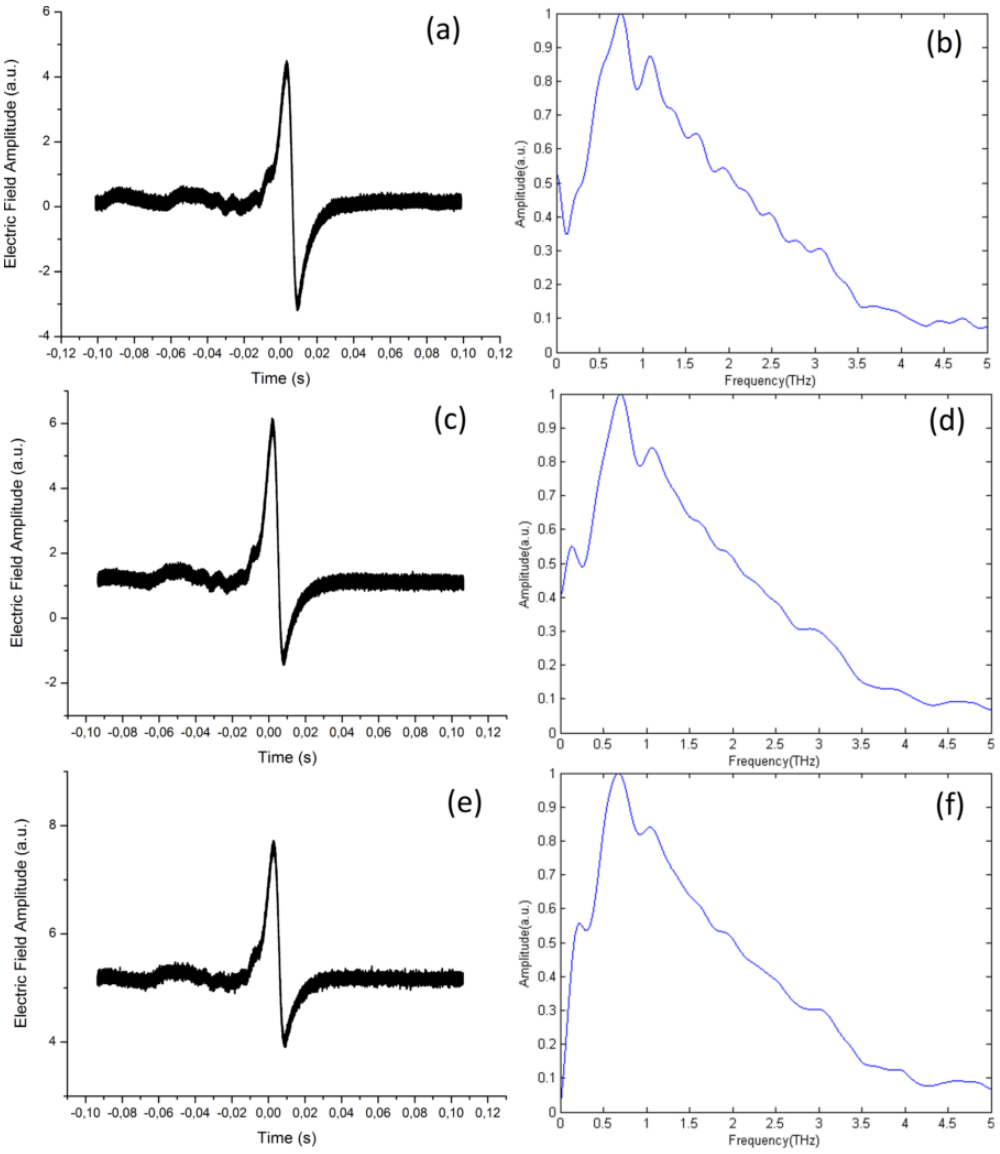

Figure 4.11: (a), (c) and (e) are the electric fields measured by the oscilloscope and (b), (d) and (f) are normalized Fourier transforms of (a), (c) and (e). In the case of (a) and (b) the sensitivity of the lock-in amplifier was set to 500 μV and the time constant was set to 30 ms, 6 dB. For (c) and (d) the sensitivity of the lock-in amplifier was set to 50 μV and the time constant was set to 300 ms, 6 dB. For (e) and (f) the sensitivity of the lock-in amplifier was set to 10 μV and the time constant was set to 3 s, 6 dB.

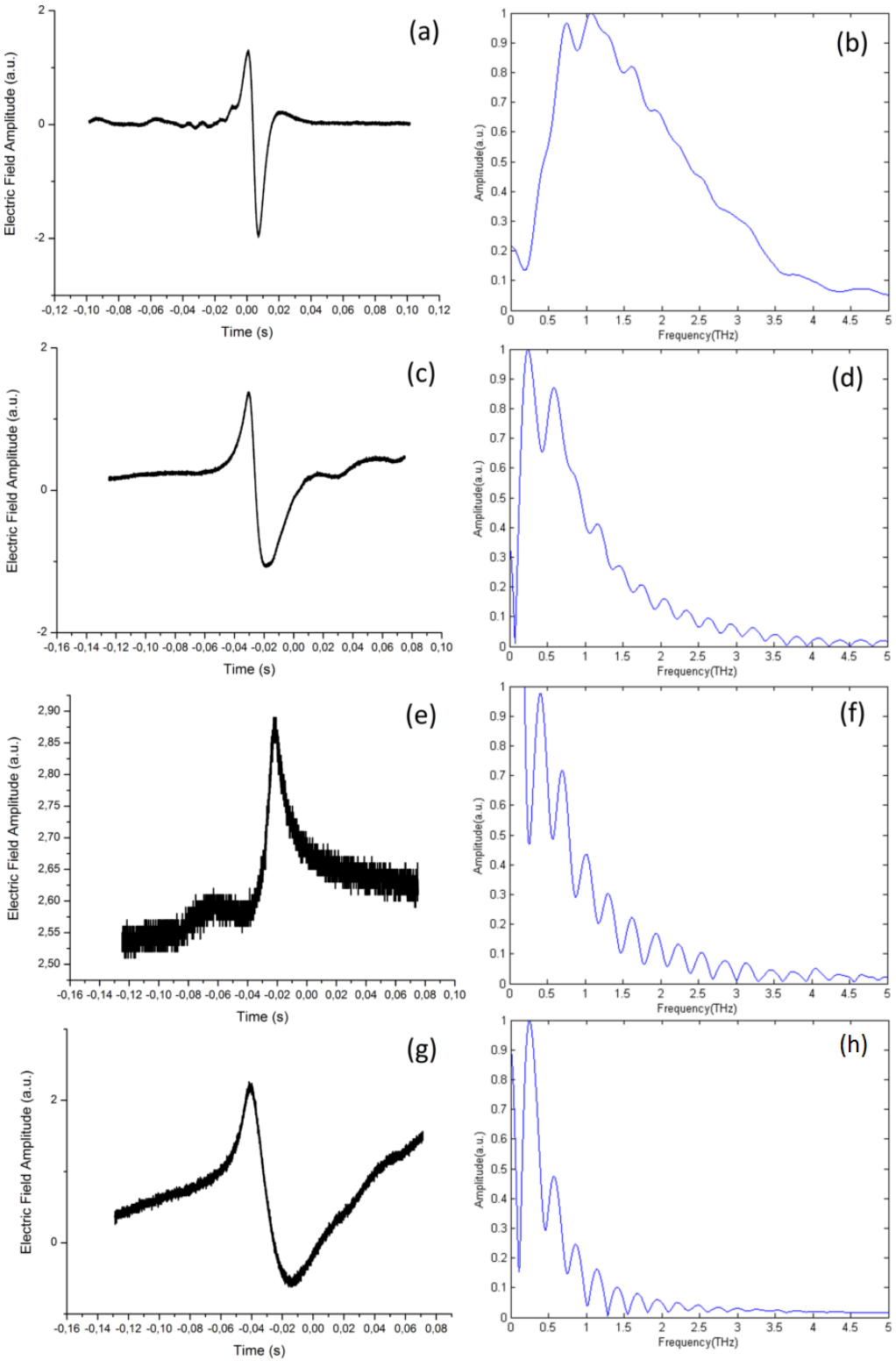

Figure 4.12: (a), (c), (e) and (g) are the electric fields measured by the oscilloscope and (b), (d), (f) and (h) are normalized Fourier transforms of (a), (c), (e) and (g). In the case of (a) and (b) the sensitivity of the lock-in amplifier was set to 5 mV and the time constant was set to 3 ms, 12 dB. For (c) and (d) the sensitivity of the lock-in amplifier was set to 200 μV and the time constant was set to 30 ms, 12 dB. For (e) and (f) the sensitivity of the lock-in amplifier was set to 20 μV and the time constant was set to 300 ms, 12 dB. For (g) and (h) the sensitivity of the lock-in amplifier was set to 50 μV and the time constant was set to 30 ms, 18 dB.

From the measurements depicted in figures 4.11 and 4.12 a few conclusions can be made. Firstly, if the slope is set lower it can result in measurements with a higher amplitude, but these measurements also then contain more noise. Secondly, if the slope is set too high it can result in a loss of measurement accuracy, since part of the signal might get filtered out. And lastly, the amplitude of the measurement can be increased by decreasing the time constant, but this will only work till a certain point.

These measurements were performed to help with the alignment process. When starting out it would be best to work with as low a slope setting and time constant as possible, since these would allow for even a weak signal from the pulse to be amplified. A higher slope is useful when working to enhance the signal once found, since it helps smooth the function so that easier optimization is possible. After alignment, different settings will be used, since the pulse measuring method is different.

4.6 Alignment

In this section the alignment procedure implemented to align the terahertz setup used during this project will be described.

4.6.1 Alignment of optical setup prior to measurements

In order to to achieve optimal output from the photoconductive antennae the optical system must be aligned. This process consists of a number of sequential steps. Firstly it is preferable to have the pump light from the laser come in perpendicular to the terahertz chip that houses our antennae, since this reduces the impact of the pump beam's polarization on the photoconductive material. To achieve this the terahertz chip and Si-lens mount are removed from the adjustable antenna mounts as depicted in figure 4.13.

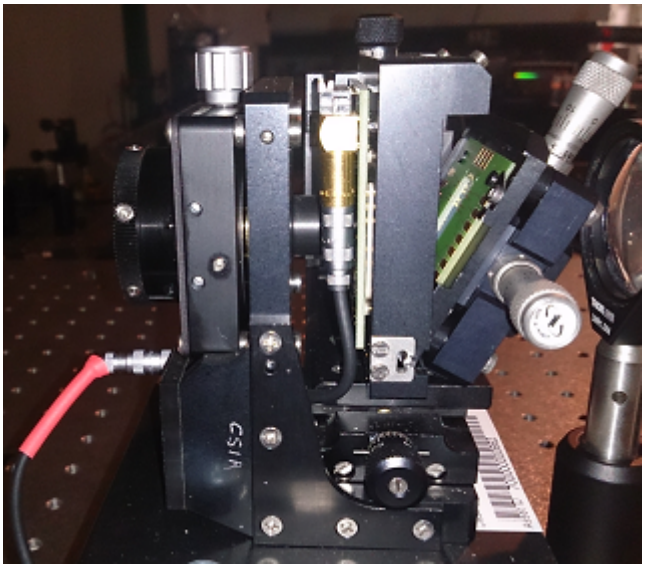

Figure 4.13: Removing antenna and Si-lens mount from adjustable antenna mounts.

Then, using mirrors M1 and M2 (as depicted in figure 4.14), the light is aligned along the optical axis of the setup. This procedure was eased via the use of an infrared viewer. This process is done for both mounting mechanisms.

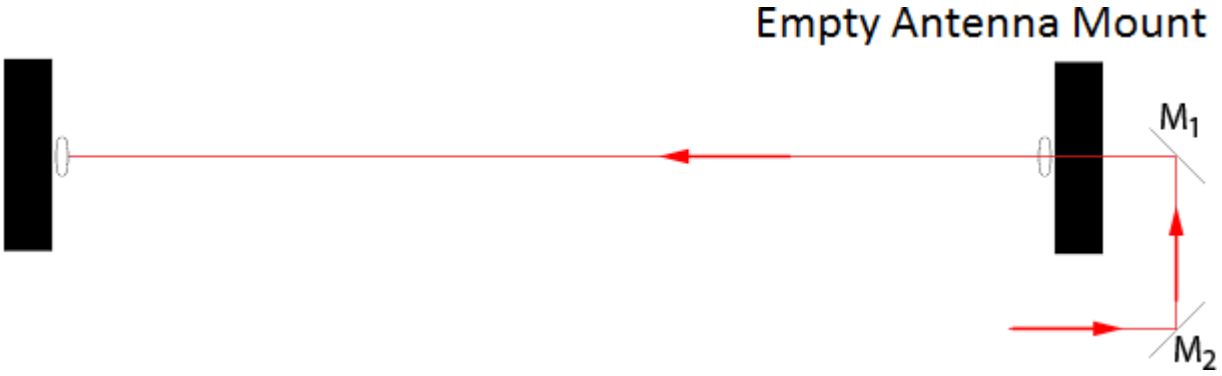

Figure 4.14: Align laser light through mount.

Having the pump light pass straight through the adjustable antenna mounts simplifies certain later processes and lowers the chances of optical effects, such as diffraction occurring near the antenna, thus also lowering losses.

Next the lenses were inserted. The lenses used are made of Polymethylpentene (TPX), which is a polymer that is transparent to both visible and terahertz radiation. The lenses used have a focal length of 40 mm. The process is eased by inserting the lenses one at a time. The lenses closest to the mounts

are inserted first (lenses L_1 and L_4 in figure 4.15). These collimate the radiation after it passes through the silicon lenses. Inserting these lenses first does seem to ease the lens alignment process as a whole somewhat. Next the inner two lenses are inserted and aligned.

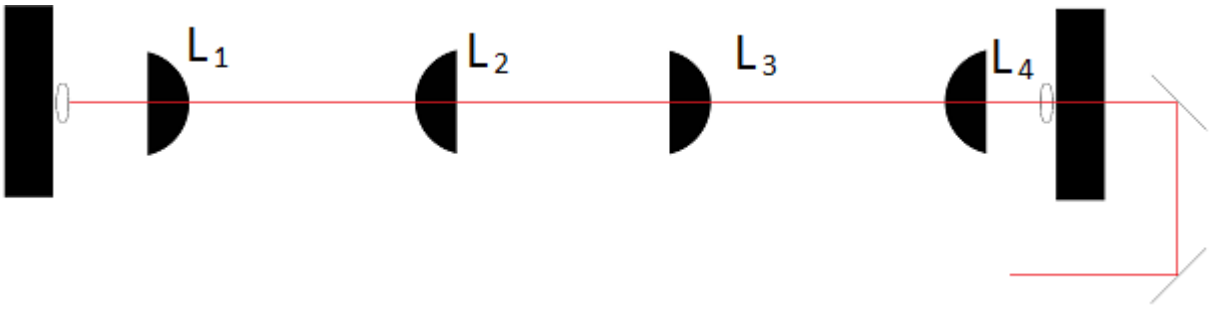

Figure 4.15: Align lenses with laser light.

Now the antenna and silicon lens mounts are inserted into the adjustable antenna mounts.

Figure 4.16: Attach the antenna mounts to the adjustable antenna mounts.

The antenna now needs to be positioned on the optical axis. A white screen with a pinhole is used to image the terahertz antenna array chip on the screen via reflection of the pump laser. Using this reflection with lens L_5 (as indicated on figure 4.16), the pump light is guided to the antenna on the chip that is intended for use. This is done for both the receiving and transmitting antenna.

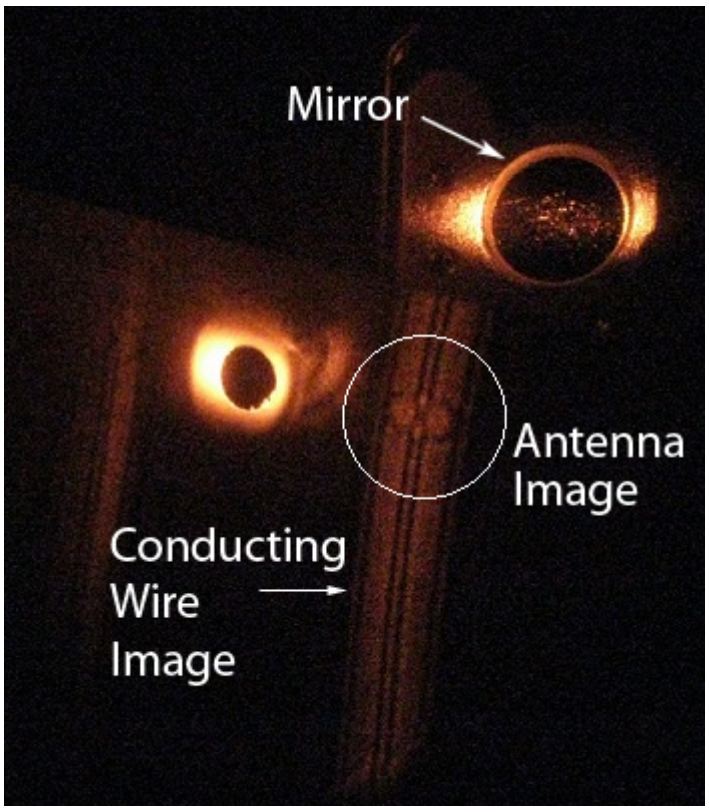

Figure 4.17: Projected reflection from terahertz chip.

Next, using a multimeter to monitor the current flowing through the antenna, the adjustable lens is used to focus the pump light on the antenna so as to achieve maximal current flow while applying a bias current to the antenna.

4.6.2 Terahertz alignment

Next the antennae must be aligned with one another. To achieve this first the optical path lengths of the two different routes to the detecting antenna had to be calculated. Based on this difference an estimate is then determined for which point on the translation stage would scan over the terahertz pulse.

For this aligning process 20 μm antennae were used as both the transmitting and receiving antennae. This was due to the central position of these antennae on the terahertz antenna array chips.

The lock-in amplifier (as introduced in section 4.5) had its slope set to 6 dB, to allow for maximal signal throughput while the signal is weak, and time constant to 100 ms, which as compromise between high amplitude and noise throughput. These settings result in a lot of noise, but also allows the signal to

be found while it is distorted and weak. The silicon lenses were then roughly aligned and scans were performed around the calculated point.

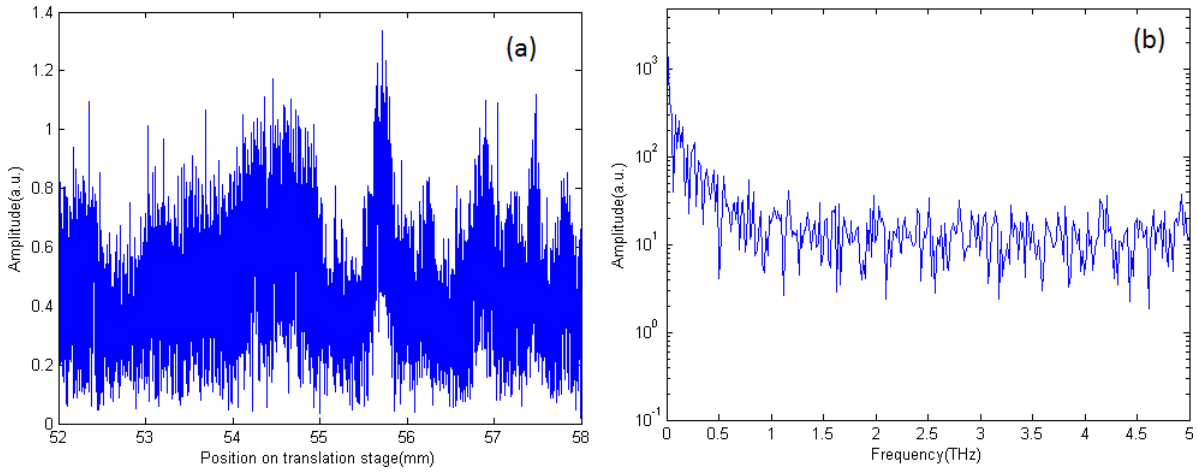

Figure 4.18: (a) The electric field measured with starting positioning of antennae with the lock-in amplifier set with a time constant of 100 ms and a slope of 6 dB and (b) an FFT taken of this data.

Next the position of the silicon lenses were adjusted so as to increase the amplitude of the pulse and to decrease the arrival time of the pulse. As the pulse amplitude increases, it becomes feasible to increase the slope setting on the lock-in amplifier. The lock-in amplifier settings were changed to a slope of 12 dB and a time constant of 300 ms. This drastically improved the signal to noise ratio.

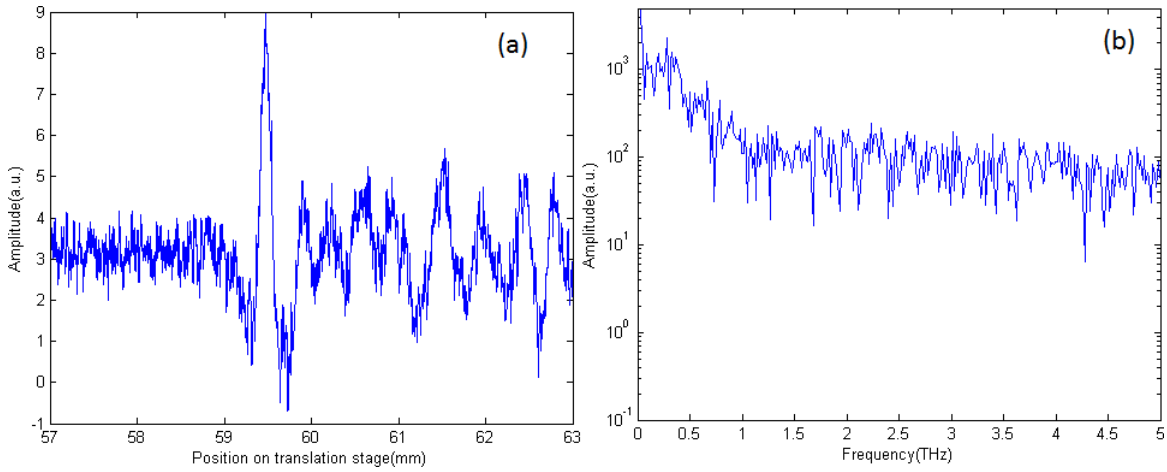

Figure 4.19: (a) The electric field measured with improved alignment of the antennae with the lock-in amplifier set with a time constant of 300 ms and a slope of 12 dB and (b) an FFT taken of this data.

Iterative adjustments were performed on the setup. First the silicon lenses are adjusted to optimize for a combination of early arrival time and maximal terahertz electric-field amplitude. Next, the lenses focusing the pump pulse on the antenna are optimized for maximal terahertz electric-field amplitude. Finally the focusing and collimating lenses between the two antennae can be optimized for a combination short pulse duration and higher terahertz electric-field amplitude.

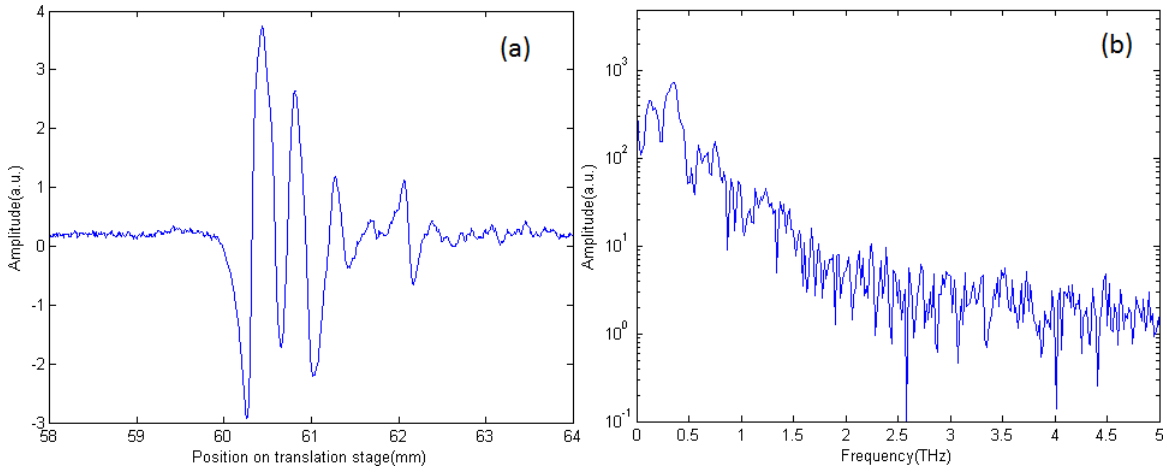

Figure 4.20: (a) The electric field measured with further adjusted positioning of antennae with the lock-in amplifier set with a time constant of 300 ms and a slope of 12 dB and and (b) an FFT taken of this data.

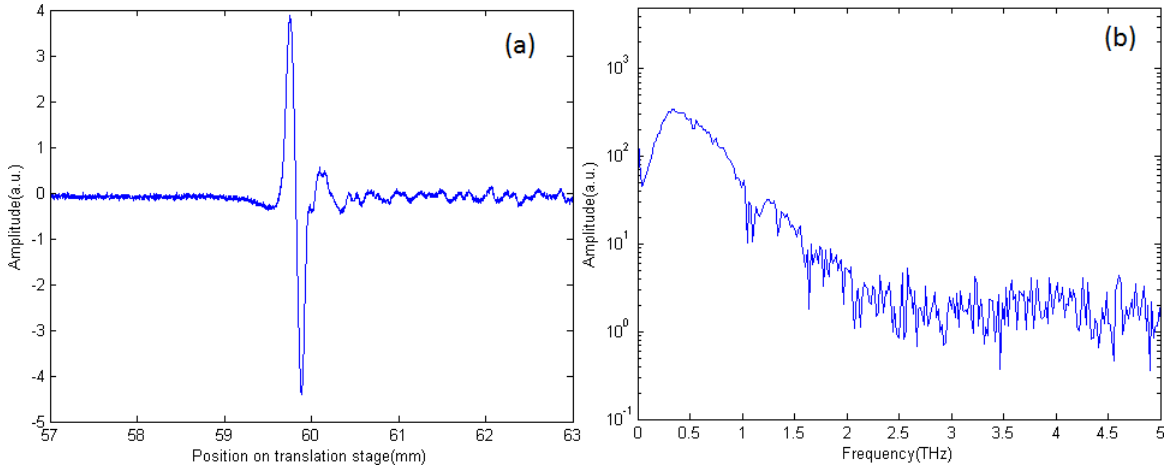

Figure 4.21: (a) The electric field measured with further adjusted positioning of antennae and adjusted lenses with the lock-in amplifier set with a time constant of 300 ms and a slope of 12 dB and and (b) an FFT taken of this data.

This iterative process is repeated until no further improvement is seen.

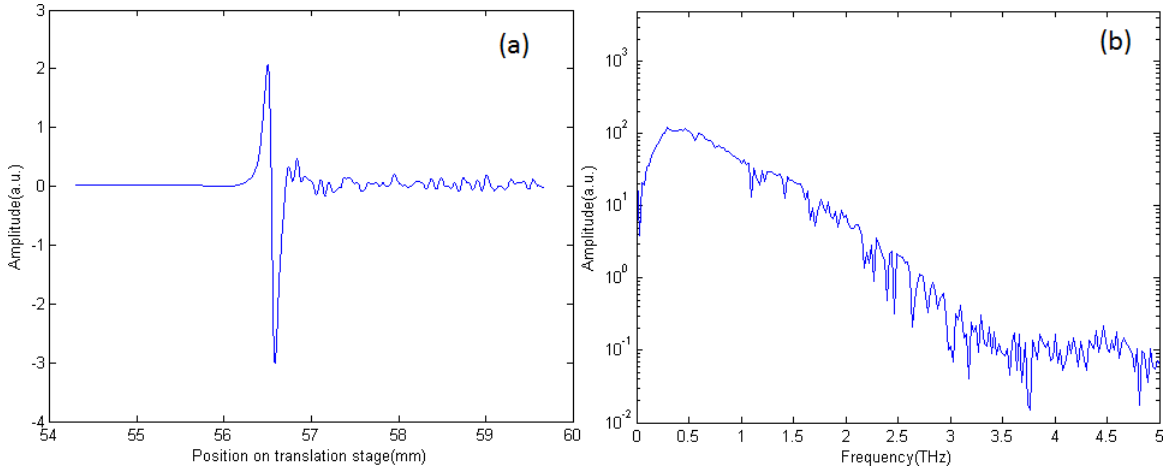

Figure 4.22: (a) The electric field measured after final adjustments to the positioning of antennae and lenses, with the lock-in amplifier set with a time constant of 30 ms and a slope of 12 dB and and (b) an FFT taken of this data.

As can be seen, upon final alignment, the signal to noise ratio is greatly improved, as well as the bandwidth of the pulse. Upon the final aligned state, the time constant was lowered, due to it having little impact on the signal to noise ratio at this point. By lowering it, it was possible to increase the speed

at which measurements were performed while still maintaining the accuracy of the measurements.

Chapter 5

Results and discussion

In this section the various results obtained during this project will be examined and discussed. In this section, both antenna characterization results and examples of terahertz time-domain spectroscopy will be shown and discussed.

5.1 Antenna characterization

In order to understand how to properly make use of the antennae used in this setup, it is important to characterize them first.

5.1.1 Antenna size dependence

In the setup used for this thesis, multiple antenna options were available, mostly varying in gap size and overall structure size. One of the objectives of this thesis was to investigate the effects of these alterations.

First measurements were taken with matched pairings of antennae.

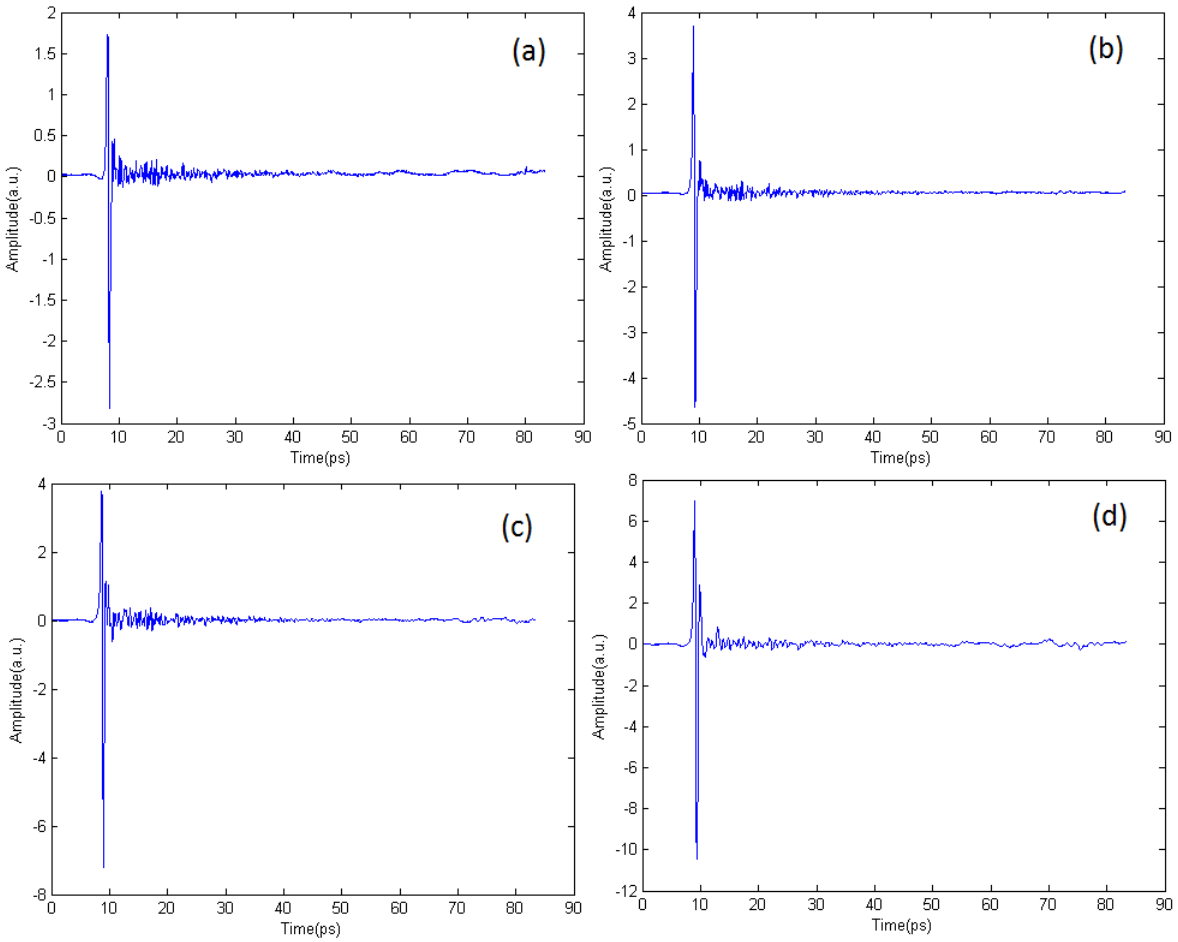

Figure 5.1: Terahertz electric field measurements in time where both the receiving and transmitting antenna are the same size. (a) is the measurement produced by a pair of antennae that have an electrode separation gap of 10 μm. (b) is the measurement produced by a pair of antennae that have an electrode separation gap of 20 μm. (c) is the measurement produced by a pair of antennae that have an electrode separation gap of 40 μm. (d) is the measurement produced by a pair of antennae that have an electrode separation gap of 60 μm.

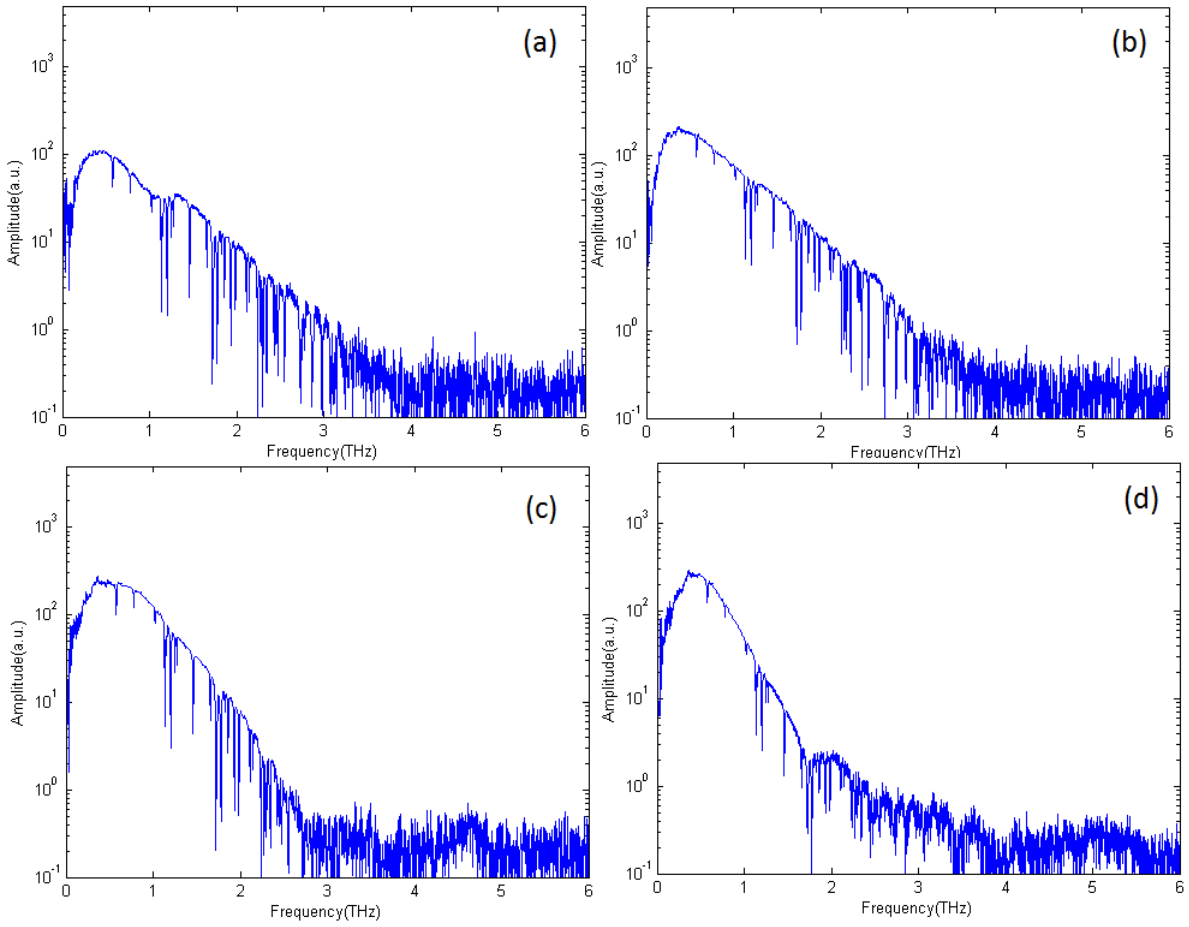

Figure 5.2: Fourier transform data for terahertz electric field measurements in time where both the receiving and transmitting antenna are the same size. (a) is the spectrum produced by a pair of antennae that have an electrode separation gap of 10 μm. (b) is the spectrum produced by a pair of antennae that have an electrode separation gap of 20 μm. (c) is the spectrum produced by a pair of antennae that have an electrode separation gap of 40 μm. (d) is the spectrum produced by a pair of antennae that have an electrode separation gap of 60 μm.

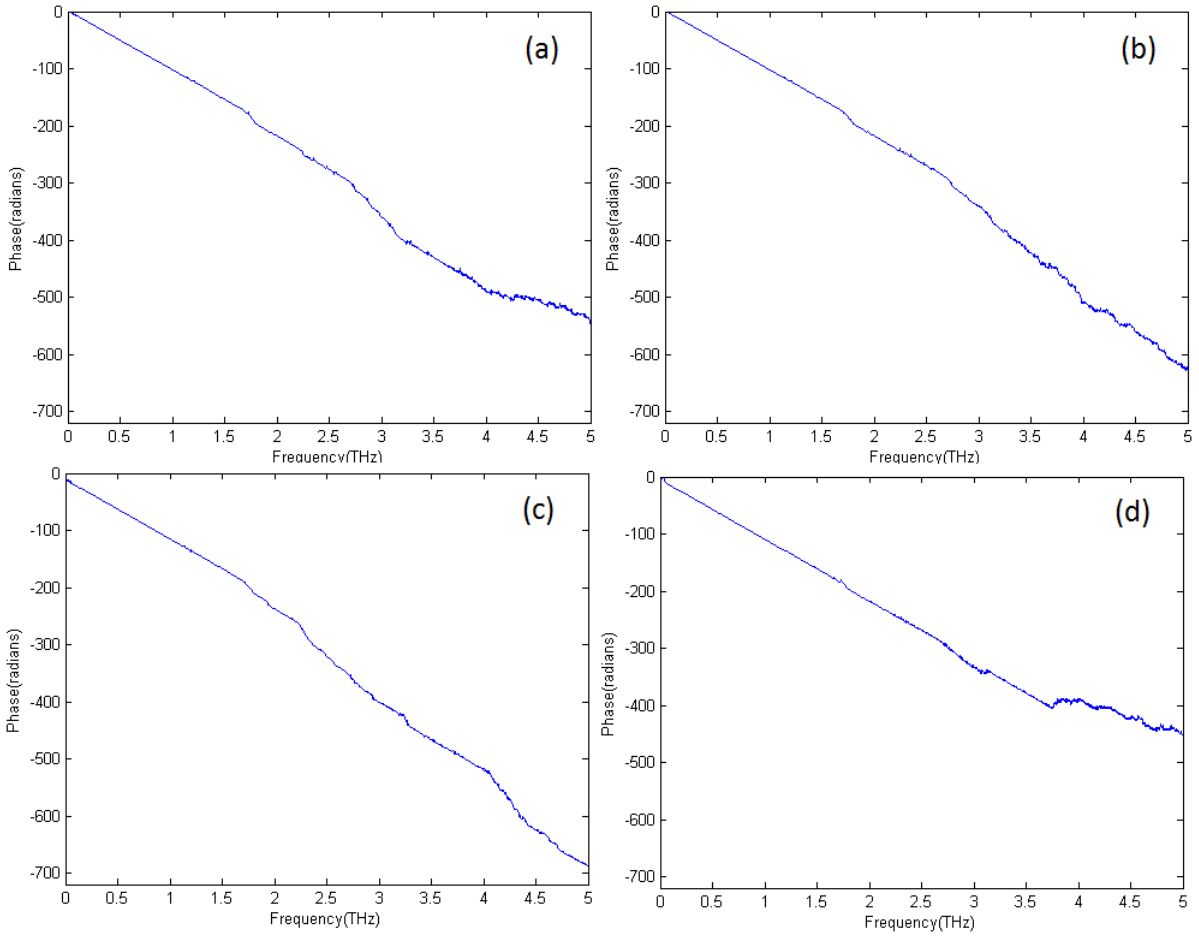

Figure 5.3: Phase data extracted from the Fourier transform data for terahertz electric field measurements in time where both the receiving and transmitting antenna are the same size. (a) is the phase extracted for a pair of antennae that have an electrode separation gap of 10 μm. (b) is the phase extracted for a pair of antennae that have an electrode separation gap of 20 μm. (c) is the phase extracted for a pair of antennae that have an electrode separation gap of 40 μm. (d) is the phase extracted for a pair of antennae that have an electrode separation gap of 60 μm.

It should be noted that in the case of the 60 μm transmitter and receiver ((d) in figures 5.1, 5.2 and 5.3), the sensitivity of the Lock-in amplifier had to be reduced by a factor of 2 due to the amplitude exceeding the sensitivity setting of the lock in amplifier. Thus on the scale of the 60 μm measurement the other measurements would be halved in amplitude.

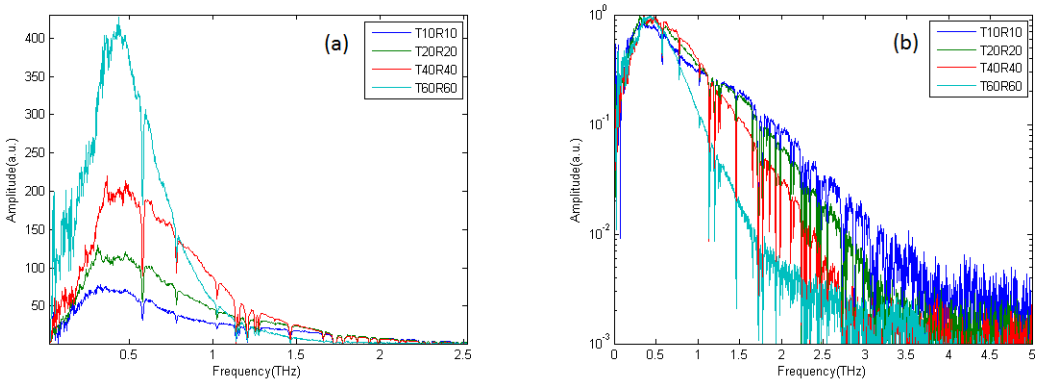

Figure 5.4: A Fourier transform taken of the electric field measured by the terahertz setup where matching sets of antennae were used. Plot (a) is on a linear scale and plot (b) is on a logarithmic scale and normalized.

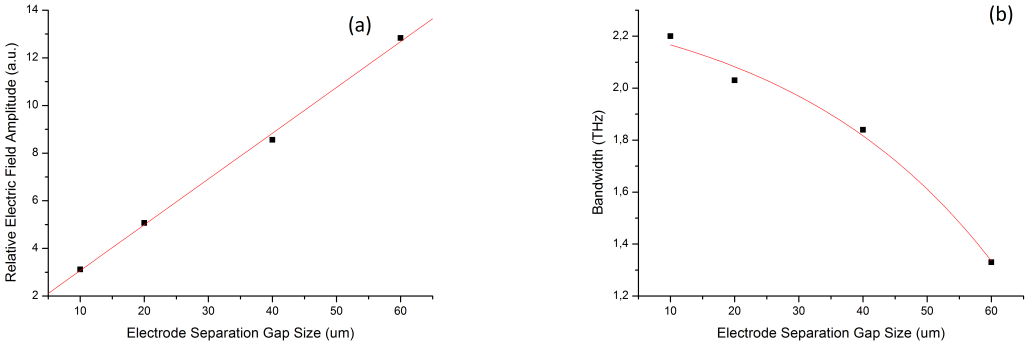

Figure 5.5: On (a) is plotted the difference between the minimum and maximum of the relative electric field amplitude over antenna electrode separation gap of the transmitting and receiving antenna, the solid line is there to help guide the eye. On (b) is plotted the FWHM of the terahertz electric field over antenna electrode separation gap of the transmitting and receiving antenna, the solid line is there to help guide the eye.

It would seem that as the electrode separation gap size is increased the generated terahertz pulse gets longer in duration, which in turn results in a narrower bandwidth. This can be explained as follows: Since the electrode separation gap is increased in size, the amount of charge carriers that are excited when the laser pumps the gap is increased. Since the overall decay time of the material is dependent on the total amount of excited charge carriers (the

system follows an exponential decay pattern), the more excited charge carriers there are, the longer it will take the system to revert back to an over-damped state.

It should be noted that these measurements have been performed in an atmospheric environment. As can be seen in figure 5.4, there are quite a few absorption lines visible in the measurements. These absorption lines are from water vapour, which has a lot of ro-vibrational absorption lines in the terahertz regime. This will be further examined in section 5.3.1.

To obtain a better idea of the role of the structural size in both the transmitting antenna and receiving antenna. A 20 μm antenna was used as a receiving antenna and then the transmitting antennae of various sizes were used and the measured terahertz electric field was examined. Similarly, a 10 μm antenna was used as a transmitting antenna and then the receiving antenna was varied and the measured terahertz electric field was examined

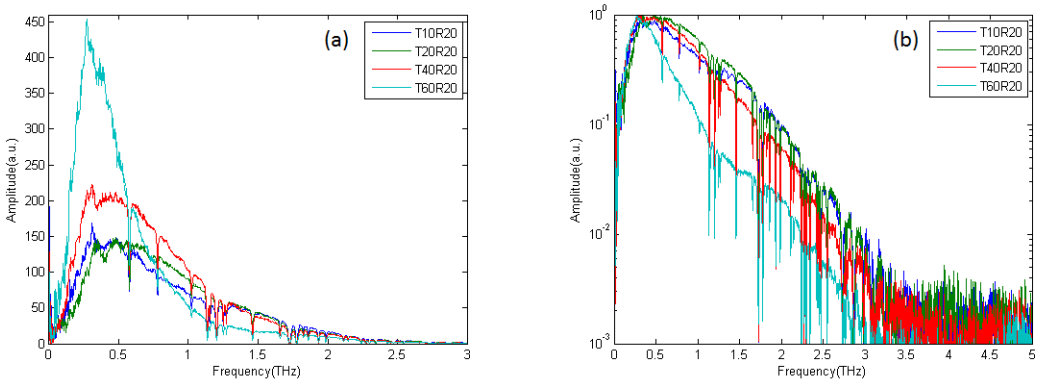

Figure 5.6: A Fourier transform taken of the electric field measured by the terahertz setup where the receiving antenna was kept constant (a 20 μm antenna) and the size of the transmitting antenna was varied ($10, 20, 40, 60\,\mu$m antennae). Plot (a) is on a linear scale. Plot (b) is on a logarithmic scale and is normalized.

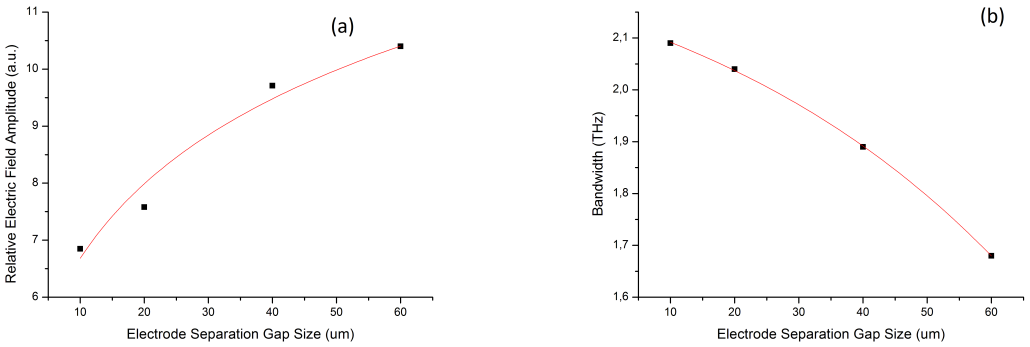

Figure 5.7: On (a) is plotted the difference between the minimum and maximum of the relative electric field amplitude over antenna electrode separation gap of the transmitting antenna, the solid line is there to help guide the eye. On (b) is plotted the FWHM of the terahertz electric field over antenna electrode separation gap of the transmitting antenna, the solid line is there to help guide the eye.

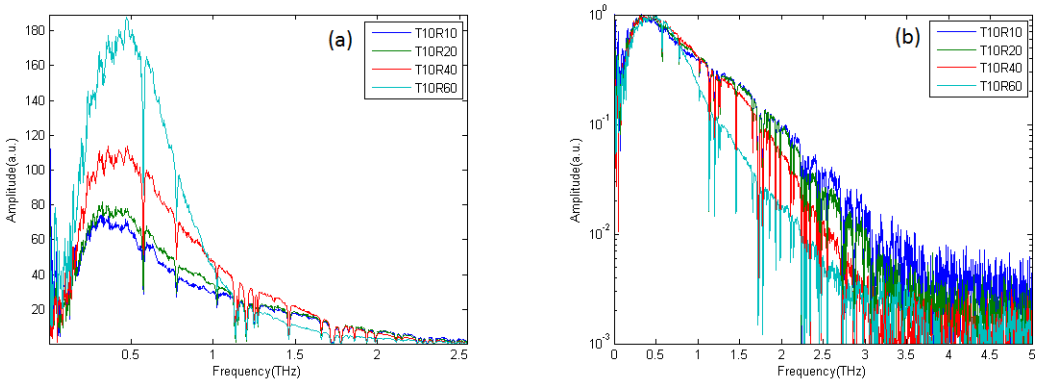

Figure 5.8: A Fourier transform taken of the electric field measured by the terahertz setup where the transmitting antenna was kept constant (a 10 μm antenna) and the size of the receiving antenna was varied ($10, 20, 40, 60\,\mu$m antennae). Plot (a) is on a linear scale. Plot (b) is on a logarithmic scale and is normalized.

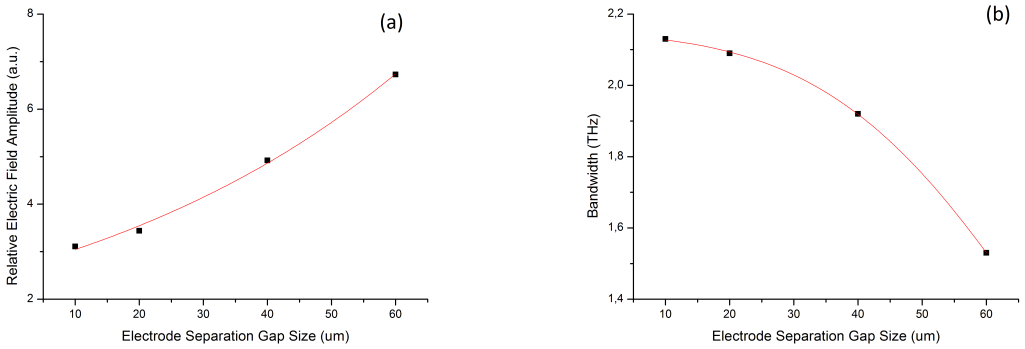

Figure 5.9: On (a) is plotted the difference between the minimum and maximum of the relative electric field amplitude over antenna electrode separation gap of the receiving antenna, the solid line is there to help guide the eye. On (b) is plotted the FWHM of the terahertz electric field over antenna electrode separation gap of the receiving antenna, the solid line is there to help guide the eye.

From figure 5.7 and 5.5 it can be seen that as the size of the electrode separation gap of either the receiving or transmitting antenna increases, so does the amplitude of the terahertz electric field measured. It can also be seen that as the electrode separation gap, of either the receiving or transmitting antenna, decreases the FWHM of bandwidth of the measured terahertz electric field increases. It would also seem from figure 5.6 that the receiving antenna might limit the measurable bandwidth.

Both the bandwidth and amplitude characteristics of the setup seem to depend on the size of both the receiving and transmitting antenna.

The one antenna array was accompanied by a manufacturer quality test. This data will be used as a rough comparison with the measured data. In this test data the tested antennae on the array were used as the transmitting antennae. The quality test data was performed with a similar pump laser. A 1 kHz, 30 V voltage was used to drive the transmitting antenna and a 20 μm antenna was used as the receiver. The quality test measurements were performed under a nitrogen flushed environment, unlike the system employed in this thesis, thus the quality test data does not show the water vapour absorption lines observed in the present data. Other details about the quality test data is unknown. This data will be compared with the data measured by the 20μm receiver as seen in figure 5.6.

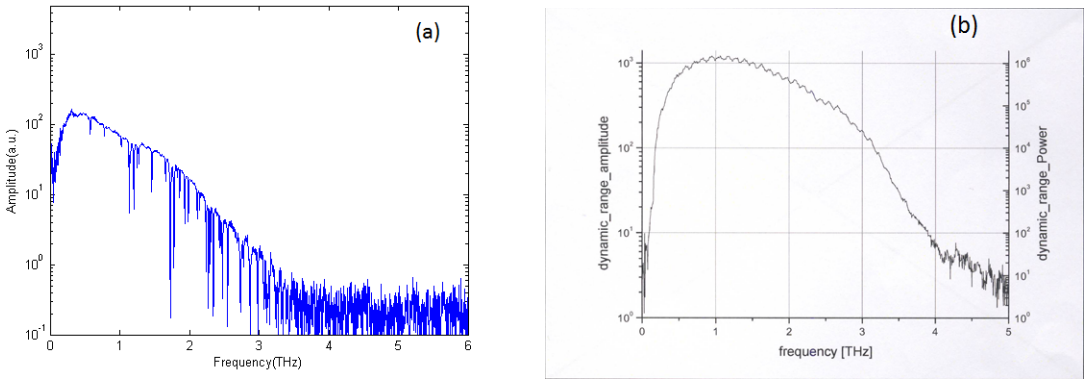

Figure 5.10: An example of the spectral data for both the quality test and measured data. These data sets are for 10 μm transmitting antennae and a 20 μm receiving antennae. (a) Measured data (b) Quality test data.

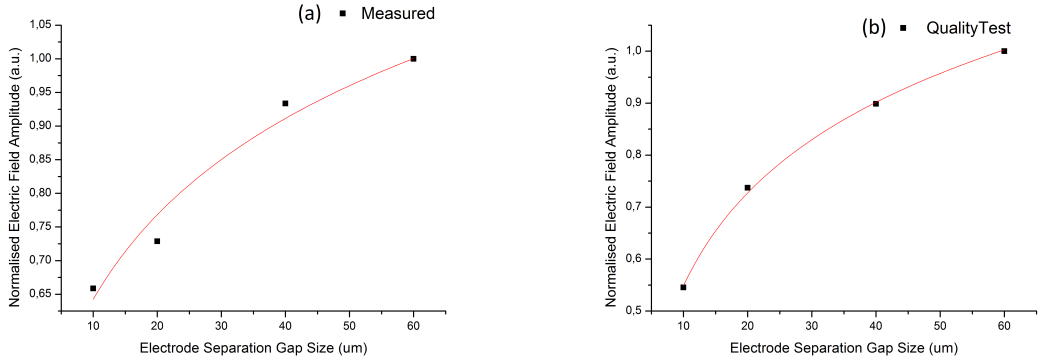

Figure 5.11: The difference between the maximum and minimum of relative amplitude of the electric field measured in time plotted over antenna electrode separation gap size and then fitted with a logarithmic function to help pull the eye. (a) Measured data (b) Quality test data.

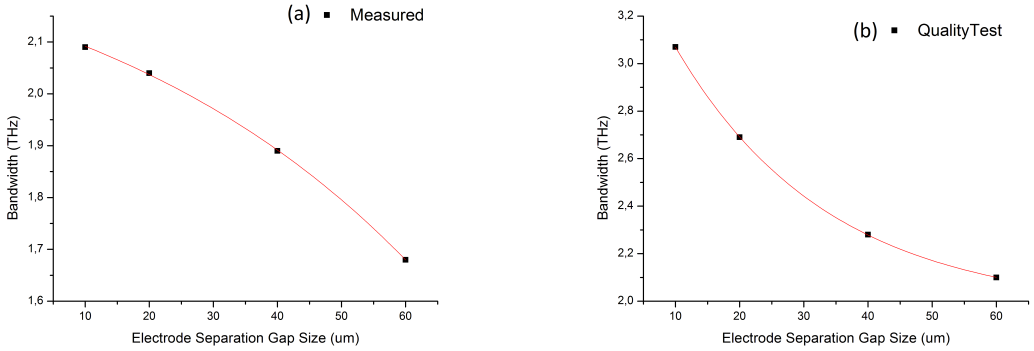

Figure 5.12: The full width at half maximum of the Fourier transform data plotted over plotted over antenna electrode separation gap size and then fitted with an exponential decay function. (a) Measured data (b) Quality test data.

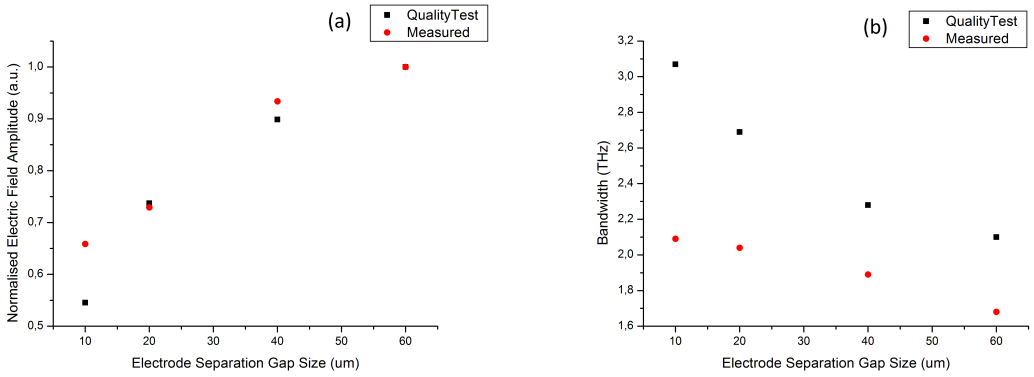

Figure 5.13: Normalized quality test data compared with the normalized measured data. On (a) is plotted the normalized data from figure 5.11 and on (b) is plotted the normalized data from figure 5.12.

As can be seen in figure 5.11, as the antenna size increases, so does the amplitude of the electric field it produces. This pattern follows a logarithmic pattern, thus indicating that there is a limit to the amount by which the amplitude will increase as the antenna size increases. Both the quality test data and measured data show this behavior.

From figure 5.12 one of two deductions can be made, since the measured and quality test data give different results. From the measured data it seems that there is an upper limit to the bandwidth of terahertz radiation that can be

generated by photoconductive antennae, where as from the quality test data it would seem that the bandwidth increases exponentially as the antenna size decreases.

When normalized, the amplitude data is quite similar, but the frequency data did show different behavior. The compared data can be seen in figure 5.13. Alignment error might account for some of the differences, but due to different experimental conditions between the two setups used to perform these measurements, it is hard to pinpoint the reason for the differences.

From these characterization results it can be deduced that for measurements where a higher intensity is favourable, such as a measurement on highly opaque samples, a larger antenna would be a better choice. When bandwidth is more important than intensity, such as during measurements on samples that do not show strong absorption of terahertz radiation, a smaller antenna would be favourable.

5.1.2 Antenna pump beam intensity dependence

Next the dependence of the measured terahertz electric field on the pump laser intensity was tested. This was done for both the receiving and transmitting antennae. During each set of measurements, the pump intensity on the one antenna is kept constant, while the other is varied, the difference between the maximum and minimum of the electric field is then plotted to examine the effect the intensity of the pump beam has on the electric field amplitude. During these measurements the polarization of the light pumped to the antennae was kept constant.

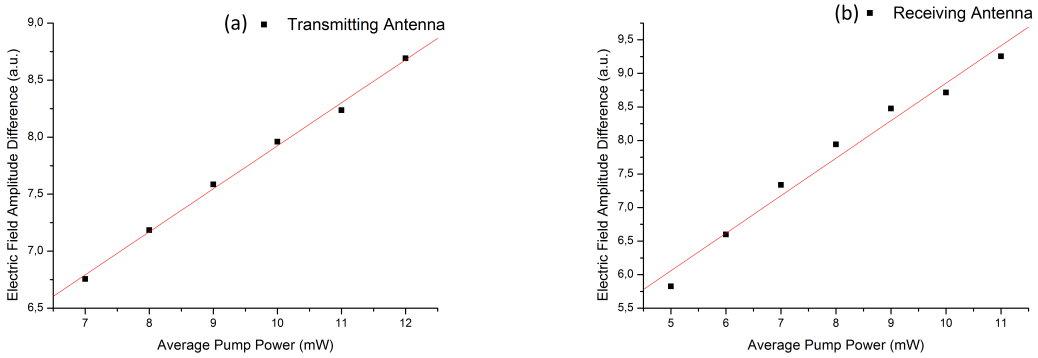

Figure 5.14: Amplitude difference between the maximum and minimum of the measured terahertz electric field plotted against pump laser intensity. In graph (a) the pump intensity for the receiving antenna was kept constant, while the average pump power on the transmitting antenna was varied. In graph (b) the average pump power for the transmitting antenna was kept constant, while the pump intensity on the receiving antenna was varied.

The antennae show a linear dependence on the average power of the incident pump pulse. The dependence on average pump power fits with what is expected when looking at equation 3.1.4 and equation 3.2.2, since according to these equations both the amplitude of the electric field produced by the transmitting antenna and the current generated by the receiving antenna are dependent on the amount of photo-excited charge carriers present. The amount of photo-excited charge carriers present in the antenna should increase linearly in the material, assuming that no non-linear processes occur, until the material starts to saturate.

5.1.3 Antenna pump beam polarization dependence

The dependence of the measured terahertz electric field on the pump laser polarization was also tested. This was also done for both the receiving and transmitting antennae. During these measurements the pump intensity was kept constant while the polarization was varied. This was done by using linear polarized light and then rotating its polarization using a halfwave plate.

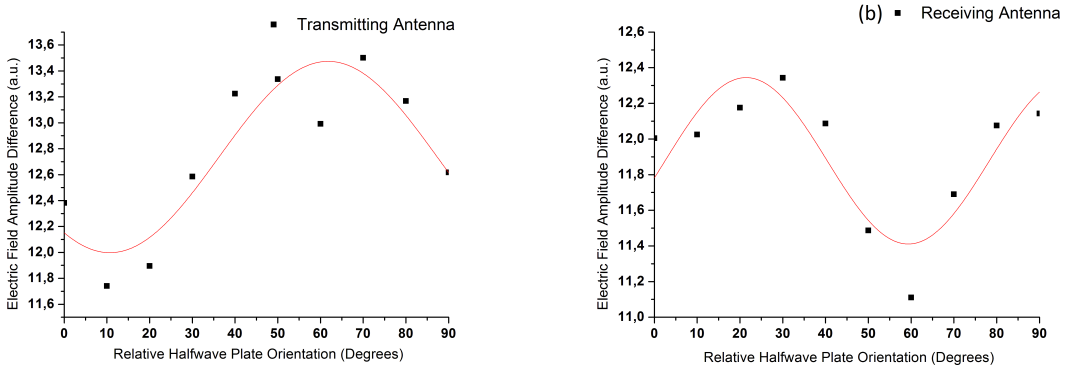

Figure 5.15: Amplitude difference between the maximum and minimum of the measured terahertz electric field plotted against pump polarization in terms of the relative orientation of the halfwave plate used. In graph (a) the pump polarization for the receiving antenna was kept constant, while the pump polarization on the transmitting antenna was varied. In graph (b) the pump polarization for the transmitting antenna was kept constant, while the pump polarization on the receiving antenna was varied.

The measured terahertz electric field show a sin squared dependence on the polarization of the incident pump pulse. These data sets are at a maximum where the pump beam is polarized perpendicular to the antenna. This could possibly be due to how the remainder of the pump pulse drives the electrons that have already been excited by the first part of the pulse, but this is purely speculation.

5.2 Effect of scan length on spectral resolution

According to Fourier theory, the spectral resolution of a Fourier transform on a set of time-domain data can be calculated from the following relation:

$$\Delta f = \frac{1}{T_0} \tag{5.2.1}$$

where T_0 is the sampling time [17]. Thus as the sampling time increases, a directly equivalent increase should occur in the frequency resolution of the Fourier transform.

To find out the degree to which the spectral resolution of the setup is affected by scan length, and more specifically to what extent absorption peak resolution is affected by scan length, measurements with different scan lengths (the distance the retro-reflector has to travel on the translation stage) were taken, using 10 μm antennae as both the transmitting and receiving antenna.

After a Fourier transform was performed on the time data, the first three peaks in the produced spectrum were zoomed in on to examine out of how many data points they comprised. These peaks are from the water vapour present in air.

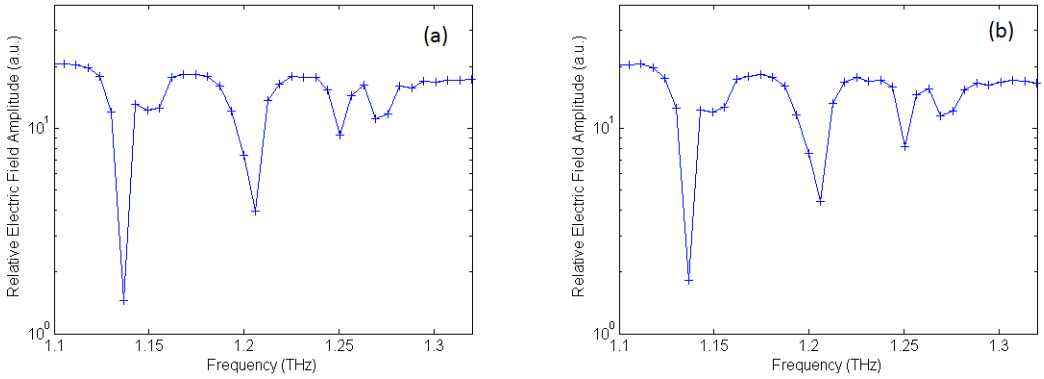

Figure 5.16: First three peaks in the Fourier transform of the measured time data. Plot (a) was produced by taking a measurement over a space of 15 mm (50 ps) and plot (b) was produced from a measurement performed over a length of 20 mm (67 ps).

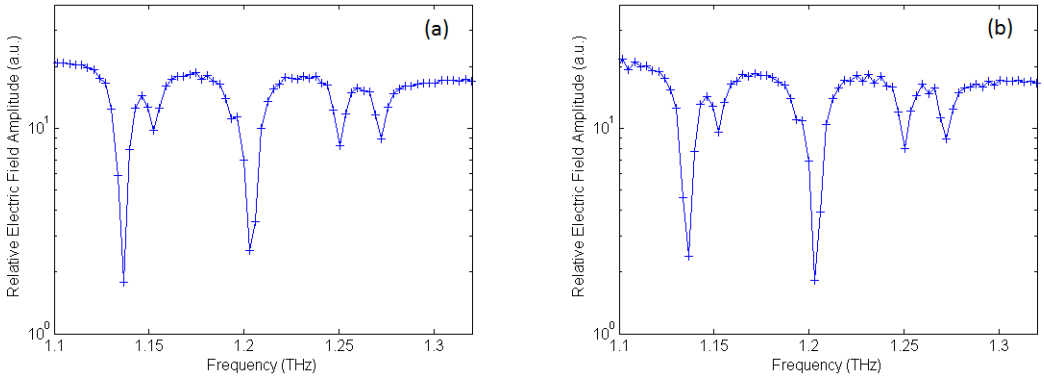

Figure 5.17: First three peaks in the Fourier transform of the measured time data. Plot (a) was produced by taking a measurement over a space of 25 mm (83 ps) and plot (b) was produced from a measurement performed over a length of 30 mm (100 ps).

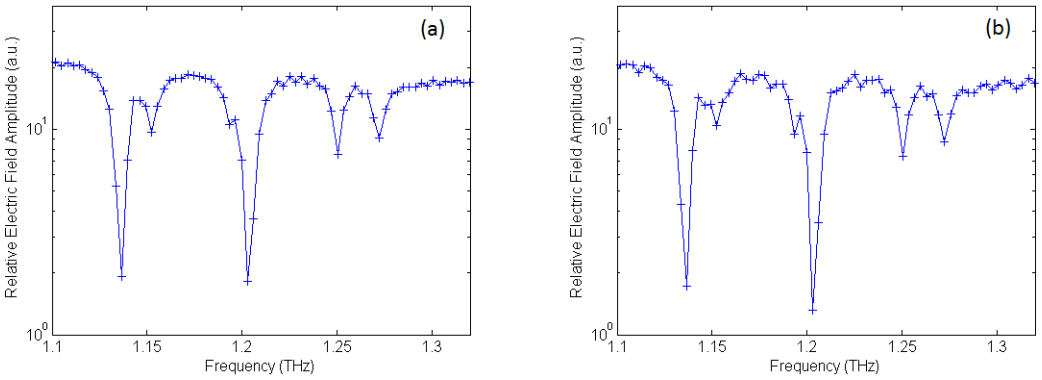

Figure 5.18: First three peaks in the Fourier transform of the measured time data. Plot (a) was produced by taking a measurement over a space of 35 mm (117 ps) and plot (b) was produced from a measurement performed over a length of 40 mm (133 ps).

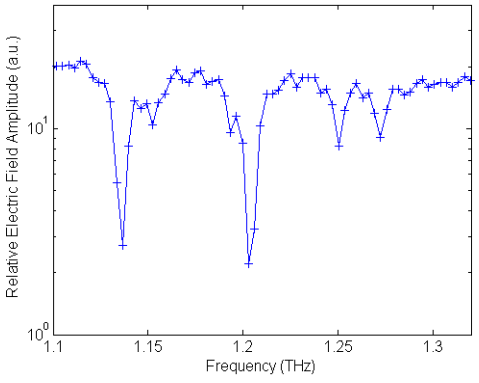

Figure 5.19: First three peaks in the Fourier transform of the measured time data. The time data was measured over a length of 45 mm (150 ps).

In 15 mm and 20 mm cases (figure 5.16) two of the peaks comprised of only three data points, namely the edge points and the peak point. Although this is feasible for imaging or a preview, it is not well suited for spectroscopy due to a lack in definition. In the cases where the scans were 25 mm or longer it was found that peaks consisted of at least five data points (figures 5.17, 5.18 and 5.19). This is an adequate resolution for spectroscopic purposes, since it helps to clarify whether an absorption peak is truly present and not an error or artifact. Further, from figures 5.18 and 5.19, it can be seen that certain data points become better resolved, but only by a small amount as the scans

start to exceed 25 mm, which means that longer scans can be taken when higher resolution is needed. It would seem that taking measurements of 25 mm in scan length is a preferable option for both resolution and measurement duration.

5.3 Examples of terahertz time-domain measurements

A few measurements were performed on samples to demonstrate the capabilities of the system. Measurements were performed on the water vapour, sugar and silicon. For the cases of sugar and the background measurement the data extraction technique described in section 2.7 was implemented to extract the frequency dependent complex refractive index information from the measured data. To perform these calculations, a measurement of the pulse in a nitrogen flushed environment was used as a reference measurement. The environment was flushed with nitrogen to remove water vapour from the terahertz radiation path.

Since the samples that will be examined are not too strongly absorbant in the terahertz spectrum, a broader bandwidth is a higher priority than a high amplitude. Accordingly, 10 μm antennae were used as both the receiving and transmitting antennae. The measurements were taken with a 25 mm scan length, since it provides sufficient spectral resolution for the measurements that were performed.

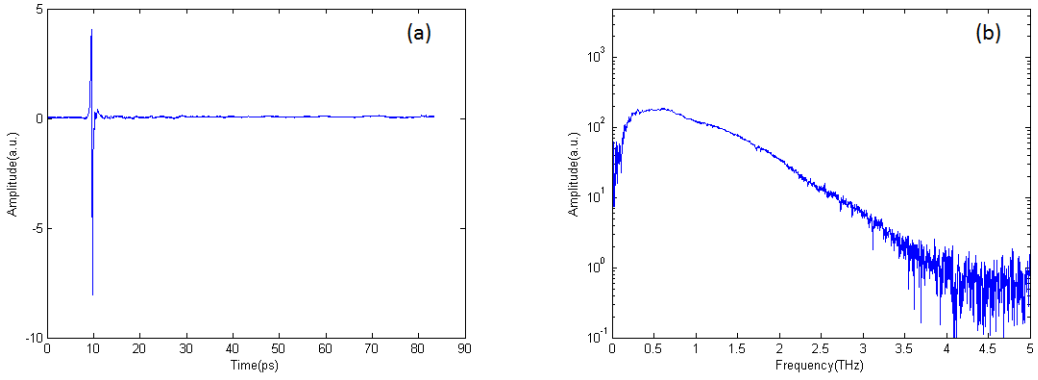

Figure 5.20: (a) Terahertz time-domain pulse measured in a nitrogen flushed environment. (b) Fourier transform of time-domain data of terahertz pulse in a nitrogen flushed environment.

5.3.1 Water vapour

To examine the water vapour present in the atmosphere a measurement was taken with no sample present and without flushing the system.

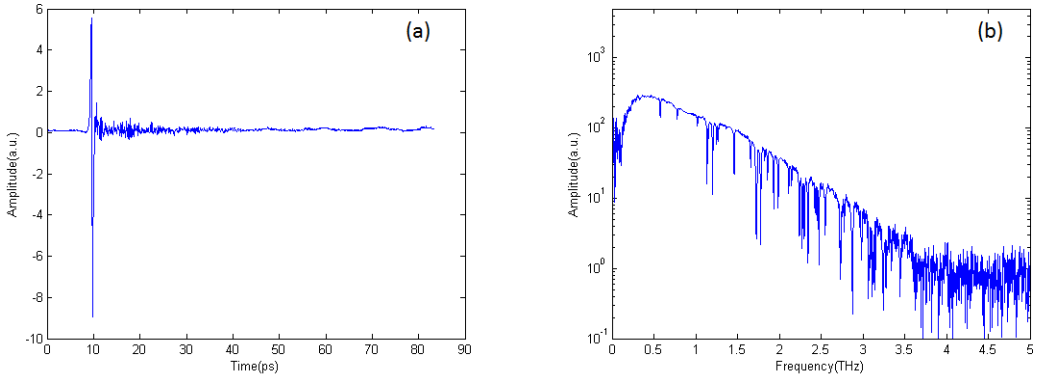

Figure 5.21: (a) Terahertz time-domain pulse measured in an unflushed environment. (b) Fourier transform of time-domain data of terahertz pulse in an unflushed environment.

Using the method as explained in section 2.7 the frequency dependent complex refractive of the background was extracted.

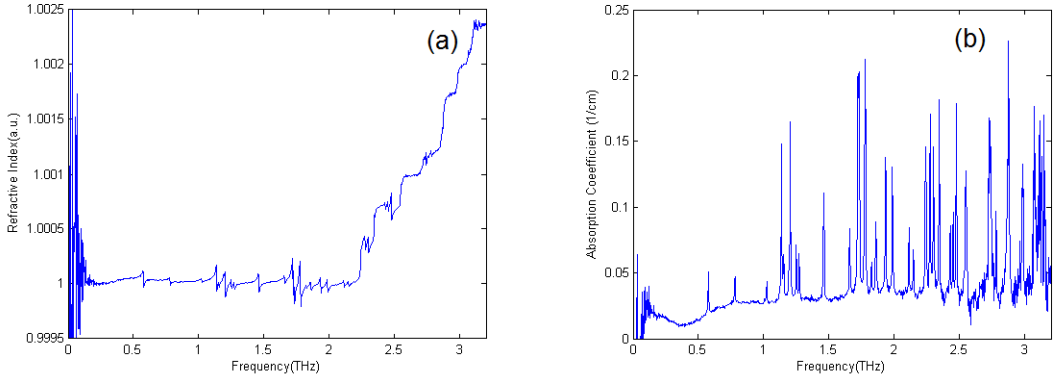

Figure 5.22: (a) water vapour refractive index. (b) Water vapour absorption coefficient.

As was explained earlier, normally the system is flushed with nitrogen. This is predominantly done to remove water vapour from the system, which is what is producing most of the resonances visible in these results, since it

has many ro-vibrational absorption lines in the terahertz region. From these results it is easy to see why it is preferable to flush the system with nitrogen when examining samples, since this greatly helps simplify the results for data extraction.

5.3.2 Sugar

A measurement was performed on a sugar crystal layer of 300 μm in thickness. This measurement was performed in a nitrogen flushed environment.

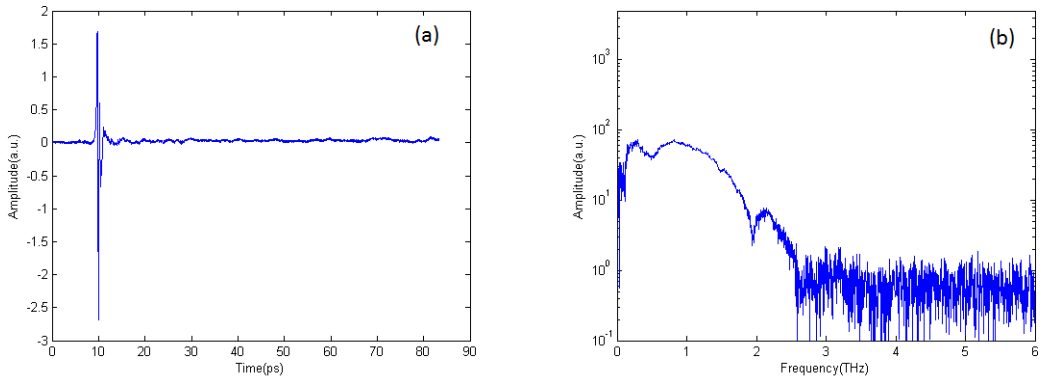

Figure 5.23: (a) Terahertz time-domain pulse measured in a flushed environment with a 300 μm sugar sample present. (b) Fourier transform of time-domain data of terahertz pulse.

Using the ratio of the transmitted electric field with respect to the reference electric field, (as explained in section 2.7) the frequency dependent complex refractive of the background was extracted.

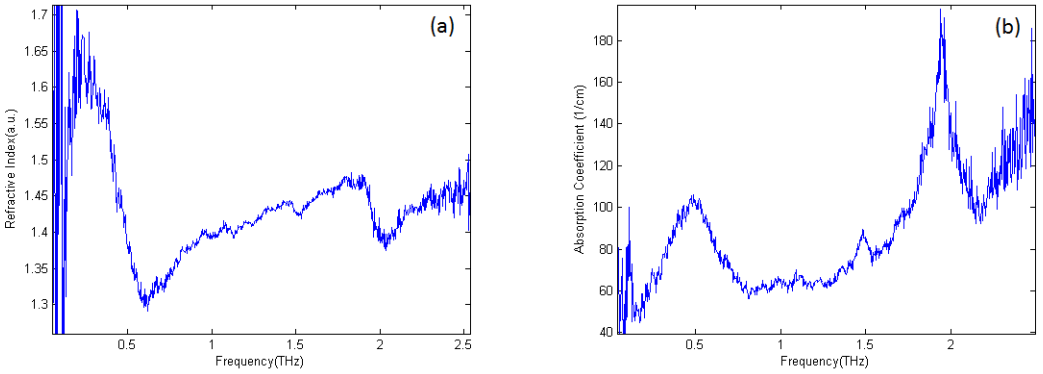

Figure 5.24: (a) Sugar refractive index. (b) Sugar absorption coefficient.

There are two rather prominent and broad resonances visible in the extracted data at 0.5 THz and 1.9 THz, and a smaller resonance is visible at

1.5 THz. From these data sets it can be seen that sugar has ro-vibrational states in the terahertz region.

5.3.3 Silicon

A measurement was performed on a 300 μm silicon sample. This measurement was performed in a nitrogen flushed environment.

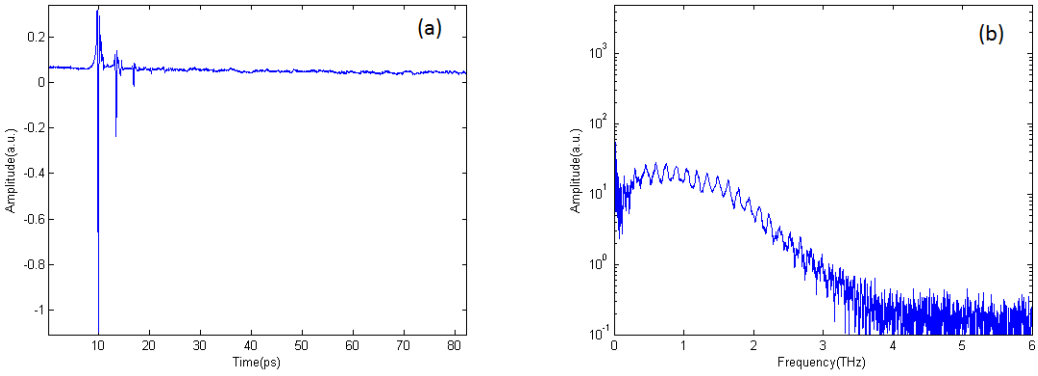

Figure 5.25: (a) Terahertz time-domain pulse measured in a flushed environment with a 300 μm silicon sample present. Due to internal reflections in the sample, multiple reflections are visible. (b) Fourier transform of time-domain data of terahertz pulse in a flushed environment with a 300 μm silicon sample present. There are oscillations visible in the spectrum.

Silicon has a rather high refractive index (3.418) and a rather low absorption coefficient (less than 0.05 cm^{-1}) in the terahertz region [18]. These result in multiple peaks being visible in the time data in figure 5.25. These other peaks are known as etalon reflections and are caused by back and forth reflections inside the sample before exiting. This effect can better be understood by looking at the Fresnel equations (equations 2.4.13 and 2.4.14), which show that at each interface between two materials with different refractive indices part of the light will be transmitted and part will be reflected. This then leads to light being reflected inside the sample with part of it being transmitted each time it comes to the boundary of the material, and thus results in multiple peaks being visible in the time data, with each peak spaced from the one before it by the amount of time it takes light to travel twice through the thickness of the material. Unfortunately these reflections result in artifacts when performing a Fourier transform on the data, as can be seen in the frequency data of figure 5.25.

Using the space between the peaks a rough average refractive index can be calculated using equation 2.5.1. Using this a refractive index value of $3.45\,(\pm 0.1)$ was calculated, which is remarkably close to the literature value of 3.418 [18].

Chapter 6

Conclusion

A terahertz time-domain spectroscopy system with multiple antennae was constructed and the antennae were characterized. Techniques were developed to align such a setup after construction, since conventional laser alignment techniques could not be used due to the wavelength that the system operates at[1]. From the results it was found that multiple factors affect measurements, such as antenna size, scan length, pump beam intensity and pump beam polarization. Pump intensity and polarization were both found to influence the amplitude of the measured terahertz electric field. Scan length affected the spectral resolution of the measurement. It was found that the electrode separation gap size of the antenna affected both the bandwidth and amplitude of the measured terahertz electric field. One conclusion to be made from the results is that the smaller antennae are more useful when a large bandwidth is needed, such as broadband spectroscopy, where as larger antennae would be preferable in situations where intensity is more important than bandwidth, such as performing measurements on optically dense samples. Using the methods described in this thesis it was also possible to extract the frequency dependent complex refractive index data for water vapour and sugar, as well as the average refractive index for silicon in the terahertz regime.

The main reason for developing this system was for its modularity, which allows for potential expansion in the near future, such as for ellipsometry or pump-probe purposes, thus broadening the potential analytical uses of the setup. These expansions will for instance allow for analysis of semiconductor and biological samples. Biological samples usually need to be suspended in an aqueous solution, which makes terahertz transmission spectroscopy a poor analysis tool for such a sample due to terahertz radiation being strongly absorbed by water. Ellipsometry provides a simplified method of conducting terahertz reflection spectroscopy.

[1]Terahertz radiation is not visible to the eye and, due to low photon energie, it is quite difficult to develop portable detectors for this frequency range.

Appendices

Appendix A

Telescope

In the setup discussed in this thesis a lens is used to focus light from the pump laser onto the photoconductive antenna. Unfortunately, the spot size of the pump laser was larger than the lens when it reached it. This is problematic, since it means not all the incoming light will be focused by the lens and some of the light might lead to unwanted effects such as diffraction.

To rectify this problem a telescope was introduced into the optical setup. The magnification of the telescope can be calculated via:

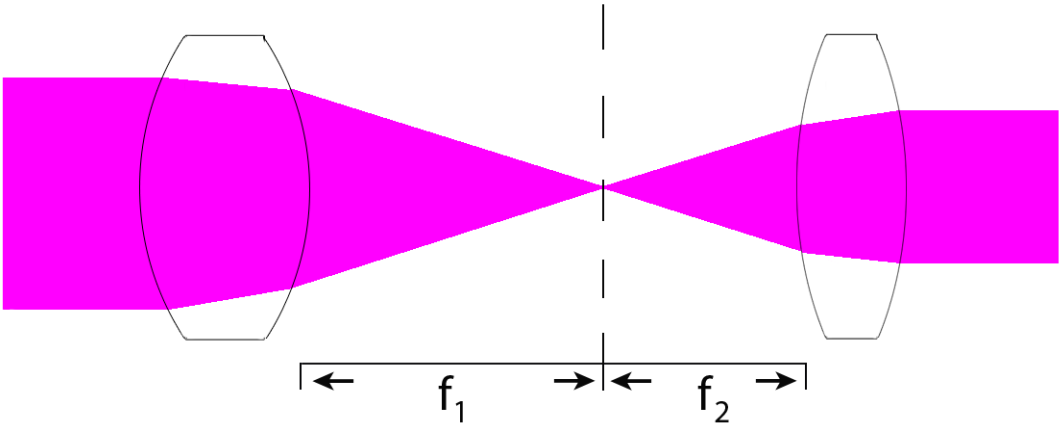

Figure A.1: Telescope: Two lenses are placed the sum of their focal lengths from one another (f_1 and f_2 are the focal lengths of the first and second lens respectively).

$$M = \frac{f_2}{f_1} \tag{A.0.1}$$

In the setup discussed, a lens with a focal length of 500 mm was paired with a lens of 300 mm. Accordingly the spot size of the pump pulse was reduced from approximately 1 cm in diameter to 0.6 mm in diameter, which is the size of the lens that focuses light onto the terahertz antenna.

Appendix B

LRC-circuit

In this section, LRC-circuits will briefly be examined. The antennae used during this thesis are LRC-circuits, and thus it is important to understand how they function.

An LRC-circuit is a circuit containing a resistor, inductor and capacitor. Due to the nature of these components the system acts like a damped harmonic oscillator for current, where the resistance is responsible for the damping.

Resonance frequency:

$$\omega_0 = \frac{1}{\sqrt{LC}}. \tag{B.0.1}$$

where L is the inductance of the circuit and C is the capacitance of the circuit.

In general LRC-circuits are considered to be in one of three states, namely underdamped, critically damped and over damped.

When a circuit is considered under damped, R (the resistance) is small enough that the system still oscillates.

When a circuit is considered critically-damped, R reaches the specific point where the system no longer oscillates.

And when a circuit is considered overdamped, R is even larger than in the critically-damped case, thus the capacitor discharges slower [19].

Since current only flows in the underdamped case, it will be more closely examined. In the underdamped case, the charge in the circuit can be represented as follows [19]:

$$q = Ae^{-(\frac{R}{2L})} \cos\left(\sqrt{\frac{1}{LC} - \frac{R^2}{4L^2}}t + \phi\right). \tag{B.0.2}$$

It can also be shown that for an underdamped LRC-circuit [19]:

$$\omega = \sqrt{\frac{1}{LC} - \frac{R^2}{4L^2}}. \tag{B.0.3}$$

The complex current for the circuit can also be derived.

The complex current is given by:

$$J = \frac{i\omega V_0 e^{-i\omega t}}{\omega^2 L + i\omega R - \frac{1}{C}}. \tag{B.0.4}$$

The physical current is given by the real component of the complex current:

$$J = \frac{V_0 \cos(\omega t - \phi)}{\sqrt{R^2 + (\omega L - \frac{1}{\omega C})^2}}. \tag{B.0.5}$$

In the case where the circuit is being driven at resonance ($\omega = \frac{1}{\sqrt{LC}}$), the physical current is given by [9]:

$$J = \frac{V_0 \cos(\omega t)}{R}. \tag{B.0.6}$$

The antennae used in this thesis are in essence LRC-circuits with a time dependent resistance. The material that forms the resistor in the circuit can be photonically excited. Normally this material has high resistivity and the system is considered to be in an overdamped state. When the material is excited using an appropriate laser source, its conductivity greatly increases and the circuit is considered underdamped. The material then rapidly returns to its groundstate and the circuit becomes overdamped again.

Appendix C

Fourier transforms

Using a Fourier transform it is possible to transform data from one domain to its reciprocal space. This is particularly useful in spectroscopy since it allows for the transformation from time-domain to frequency-domain and vice versa. In this thesis Fourier transforms were used to extract the spectral amplitude and phase data from the measured time-domain data.
The general form of the Fourier transform is given by:

$$\mathcal{F}\{f(x)\} = \int_{-\infty}^{\infty} f(x)e^{i\alpha x}dx = F(\alpha). \tag{C.0.1}$$

And the inverse Fourier transform is given:

$$\mathcal{F}^{-1}\{f(x)\} = \frac{1}{2\pi}\int_{-\infty}^{\infty} F(\alpha)e^{-i\alpha x}dx = f(x). \tag{C.0.2}$$

If one only works from 0 to ∞, which is a common case when transforming from the time-domain, then using the sin or cos transforms might be preferable since they simplify the calculations. Deciding which depends on the boundary conditions:
If $\frac{\partial f}{\partial x}\big|_{x=0} = 0$ (using $f(x, y)$) the cos transformation would be preferable, which is given by:

$$\mathcal{F}_c\{f(x, y)\} = \int_0^{\infty} f(x, y)\cos(\alpha x)dx = F(\alpha, y). \tag{C.0.3}$$

The inverse cos transform is given by:

$$\mathcal{F}_c^{-1}\{f(x)\} = \frac{2}{\pi}\int_0^{\infty} F(\alpha, y)\cos\alpha x dx = f(x, y). \tag{C.0.4}$$

It is also useful to note that:

$$\mathcal{F}_c\{f''(x, y)\} = -\alpha^2 F(\alpha, y) - f'(0, y). \tag{C.0.5}$$

Alternatively, if $f(0, y) = 0$, the sin transform would be preferable, which is given by:

$$\mathcal{F}_s\{f(x, y)\} = \int_0^\infty f(x, y) \sin(\alpha x) dx = F(\alpha, y). \tag{C.0.6}$$

The inverse sin transform is given by:

$$\mathcal{F}_s^{-1}\{f(x)\} = \frac{2}{\pi} \int_0^\infty F(\alpha, y) \sin \alpha x dx = f(x, y). \tag{C.0.7}$$

It is also useful to note that:

$$\mathcal{F}_s\{f''(x, y)\} = -\alpha^2 F(\alpha, y) + \alpha f(0, y). \tag{C.0.8}$$

[20]

C.1 Phase extraction

As was stated earlier, Fourier transforms are used to extract both the spectral amplitude and phase information from the time-domain data. In this section the extraction of the phase data will be discussed. The phase data is needed for the calculation of the frequency dependent refractive index.

It is possible to extract the phase data from Fourier transform data. This is a two step process. The first step is to extract the wrapped phase angle data from the Fourier data. There are a few methods of doing this. A simple example of a method used to do so is by taking the arctan of e^{ix}, where x is the Fourier transform data.

The second step is unwrapping the phase angle data. The phase angle data should be continuous, since a discontinuity should show itself as void in Fourier data. Phase unwrapping produces a continuous data set from the wrapped phase data. This is done by shifting the phase angle data by integer multiples of 2π.

For the purposes of thesis the Matlab function "angle()" was used to extract the wrapped phase angle data and the function "unwrap()" was used to unwrap the data [21; 22].

Appendix D

Solvents

During the course of this thesis, measurements were performed on several solvents, in order to determine which solvents would be useful for use in terahertz spectroscopy. These measurements were performed via use of a commercial terahertz time-domain spectroscopy setup;

Since these samples are fluids, they needed to be mounted in a container, an EZ-quartz cuvette, with a 1 mm gap and 1.25 mm thick sides, was used for this purpose. The cuvette causes internal reflections, since quartz has a higher refractive index in the terahertz regime than air, which can be seen in both the time-domain and spectrum.

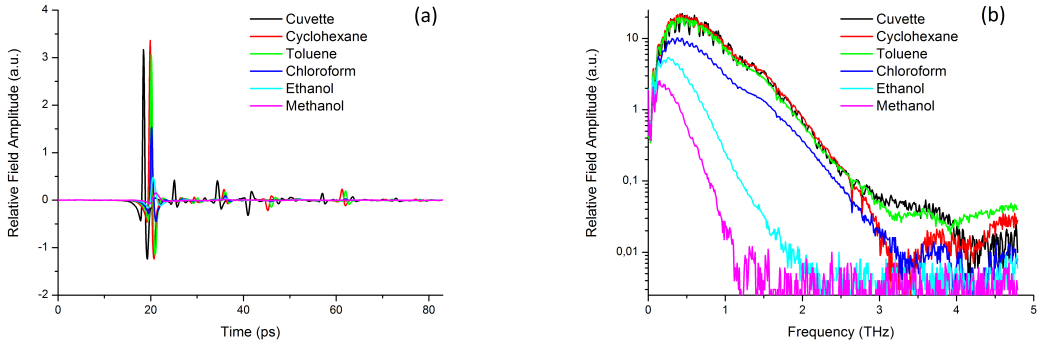

Figure D.1: Multiple solvent samples measured inside a 1 mm EZ-quartz cuvette, as well as a measurement taken of the empty cuvette. On (a) is plotted the electric field measured in time and on (b) is plotted the Fourier transform data for the associated data.

Using the ratio of the transmitted electric field with respect to the reference electric field, (as explained in section 2.7) the frequency dependent complex

refractive of the background was extracted. The cuvette measurement was used as the reference. This was done for all the measured samples.

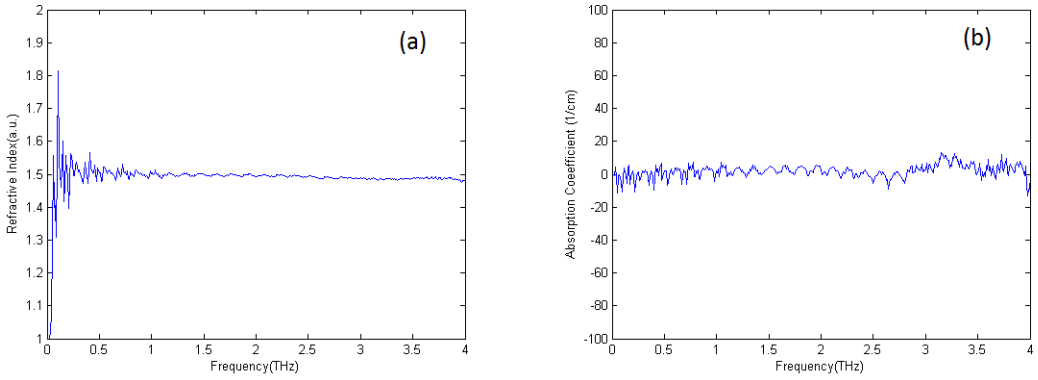

Figure D.2: (a) Toluene refractive index. (b) Toluene absorption coefficient.

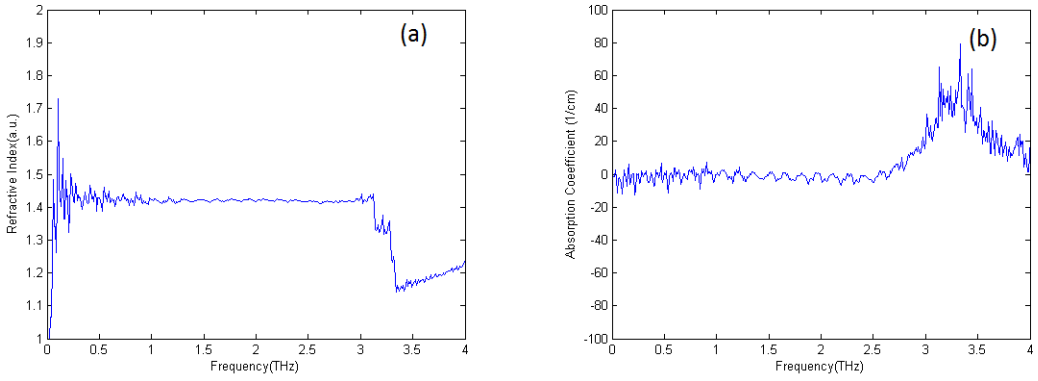

Figure D.3: (a) Cyclohexane refractive index. (b) Cyclohexane absorption coefficient.

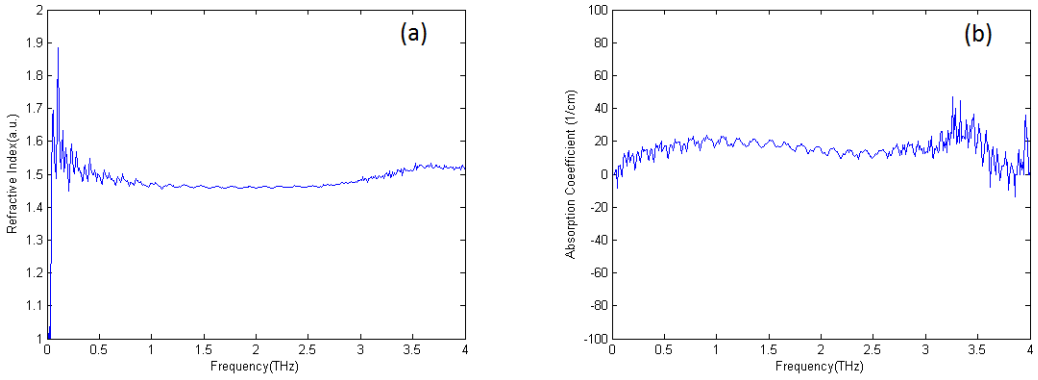

Figure D.4: (a) Chloroform refractive index. (b) Chloroform absorption coefficient.

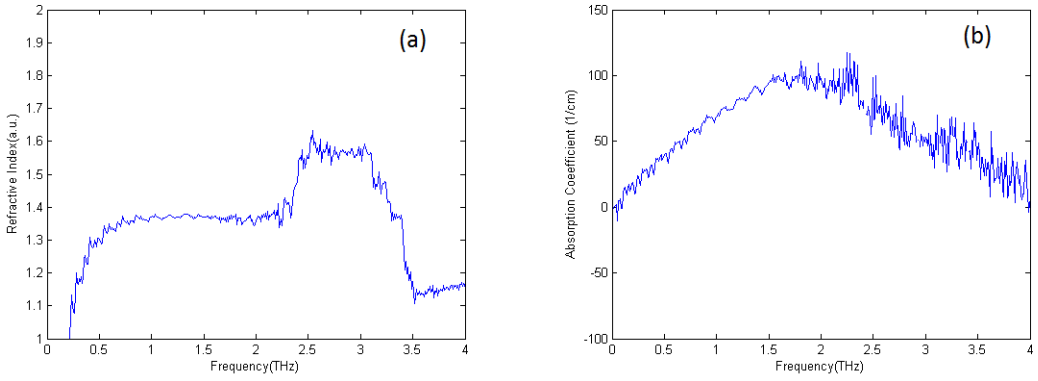

Figure D.5: (a) Ethanol refractive index. (b) Ethanol absorption coefficient.

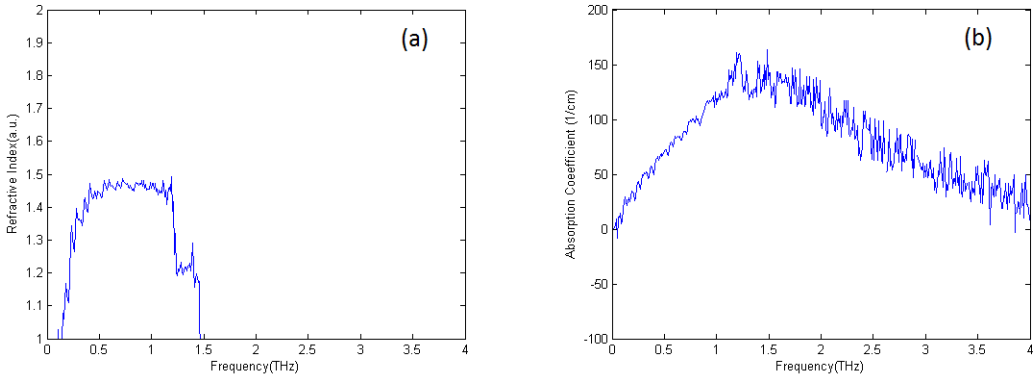

Figure D.6: (a) Methanol refractive index. (b) Methanol absorption coefficient.

It would seem that Toluene and Cyclohexane are good candidates for use during terahertz spectroscopy, due to their low absorption in the terahertz region (figure D.2 and D.3).Chloroform also has a low refractive index, but displays higher absorption than cyclohexane and toluene. (See figure D.4) From these results, it would seem that non-polar solvents are better suited for use in the terahertz regime than polar solvents[1], since the polar solvents show far higher absorption levels in the terahertz regime than the non-polar solvents. This information is useful when considering a sample that needs to be examined in a solution.

[1]Cyclohexane, toluene and chloroform are non-polar, while ethanol and methanol are polar

Bibliography

[1] Griffiths, D.: *Introduction to Electrodynamics*. 3rd edn. Pearson Education, Inc, Pearson Benjamin Cummings, 1301 Sansome St., San Francisco, CA 94111, 2008.

[2] Brodschel, A., Tauser, F., Huber, R., Sohn, J. and Leitenstorfer, A.: Amplitude and phase resolved detection of tunable femtosecond pulses with frequency components beyond 100 thz. *Ultrafast Phenomena XII*, vol. 66, pp. 215–217, 2001.

[3] Siegel, P.: Terahertz technology. *IEEE Transactions On Microwave Theory and Techniques*, vol. 50, no. 3, pp. 910–927, March 2002.

[4] Phillips, T. and Keene, J.: Submillimeter astronomy. *Proc. IEEE*, vol. 80, pp. 1662–1678, November 1992.

[5] Leisawitz, D.: Scientific motivation and technology requirements for the spirit and specs far-infrared/submillimeter space interferometers. *Proc. SPIE*, vol. 4013, pp. 36–46, March 2000.

[6] Hubers, H.: Terahertz heterodyne receivers. *IEEE Journal of S*, vol. 14, no. 2, pp. 378–391, March 2008.

[7] Sakai, K.: *Terahertz Optoelectronics*. 1st edn. Springer-Verlag, Springer-Verlag New York, LLC, 233 Spring Street, New York, NY 10013, USA, 2005.

[8] Xie, X., Dai, J. and Zhang, X.: Coherent control of thz wave generation in ambient air. *Physical Review Letters*, vol. 97, no. 075005, pp. 1–4, Febuary 2006.

[9] Ohanian, H.: *Classical Electrodynamics*. 1st edn. Allyn and Bacon, Inc, 7 Wells Avenue, Newton, Massachusetts 02159, 1988.

[10] Dressel, M. and Gruner, G.: *Electrodynamics of Solids*. Cambridge University Press, 2003.

[11] Bohren, C.: What did kramers and kronig do and how did they do it. *European Journal of Physics*, vol. 31, pp. 1–3, 2010.

[12] Lewis, R.: *Terahertz Physics*. Cambridge University Press, 2012.

[13] Ashcroft, N. and Mermin, N.: *Solid Stat Physics*. Thomson Learning, Inc., 1976.

[14] Boyd, R.: *Nonlinear Optics*. Academic Press, 2003.

[15] Lee, Y.: *Principles of terahertz science and technology*. Springer, 2009.

[16] Rulliere, C.: *Femtosecond Laser Pulses Principles and Experiments*. Springer, 2005.

[17] Seikkala, S.: Signals and systems. Spring 2000.
Available at: `http://s-mat-pcs.oulu.fi/~ssa/ESignals/sig2_2_4.htm`

[18] Grischkowsky, D.: Far-infrared time-domain spectroscopy with terahertz beams of dielectrics and semiconductors. *Journal of the Optical Society of America B*, vol. 7, no. 10, pp. 2006–2015, 1990.

[19] Sears and Zemansky: *University Physics*. 12th edn. Pearson Education, Inc, Pearson Addison-Wesley, 1301 Sansome St., San Francisco, CA 94111, 2008.

[20] Zill, D. and Cullen, M.: *Differential Equations with Boundary Value Problems*. 7th edn. Brooks/Cole, 10 Davis Drive, Belmont, CA 94002-3098, USA, 1988.

[21] Itoh, K.: Analysis of the phase unwrapping problem. *Applied Optics*, vol. 21, no. 14, p. 2470, July 1982.

[22] Ghiglia, D. and Pritt, M.: *Two-dimensional phase unwrapping theory*. John Wiley & Sons, 1998.